Paper accepted for publication at Remote Sensing of Environment
https://doi.org/10.1016/j.rse.2022.112998

Forest structure and solar-induced fluorescence across intact and degraded forests in the Amazon

Ekena Rangel Pinagé[1,2], David M. Bell[3], Marcos Longo[4,5], Sicong Gao[6,7], Michael Keller[4,8], Carlos A. Silva[9], Jean P. Ometto[10], Philipp Köhler[11], Christian Frankenberg[11], Alfredo Huete[1]

[1] School of Life Sciences, University of Technology Sydney, Ultimo, NSW 2007, Australia. E-mail address: ekena.rangelpinage@student.uts.edu.au; alfredo.huete@uts.edu.au

[2] College of Forestry, Oregon State University, Corvallis, OR 97333, USA. E-mail address: rangelpe@oregonstate.edu

[3] Pacific Northwest Research Station, USDA Forest Service, Corvallis, OR 97333, USA. E-mail address: david.bell@usda.gov

[4] Jet Propulsion Laboratory, California Institute of Technology, Pasadena, CA 91109, USA. E-mail address: mdplongo@gmail.com

[5] Climate and Ecosystem Sciences Division, Lawrence Berkeley National Laboratory, Berkeley, CA 94720, USA. E-mail address: mlongo@lbl.gov

[6] Centre for Applied Water Science, Faculty of Science and Technology, University of Canberra, Canberra, ACT 2617, Australia. E-mail address: steve.gao@canberra.edu.au

[7] Land and Water, Commonwealth Science and Industrial Research Organisation (CSIRO), Urrbrae, SA 5064, Australia

[8] International Institute of Tropical Forestry, USDA Forest Service, Río Piedras 00926, Puerto Rico. E-mail address: mkeller.co2@gmail.com

[9] School of Forest, Fisheries and Geomatics Sciences, University of Florida, Gainesville, FL 32611, USA.

E-mail address: c.silva@ufl.edu
[10] Earth System Science Center, National Institute for Space Research, São José dos Campos, SP 12227-010, Brazil. E-mail address: jean.ometto@inpe.br
[11] Division of Geological and Planetary Sciences, California Institute of Technology, Pasadena, CA 91109, USA. E-mail addresses: pkoehler@caltech.edu; cfranken@caltech.edu
Corresponding Author: Ekena Rangel Pinagé, rangelpe@oregonstate.edu

Abstract

Tropical forest degradation (e.g., anthropogenic disturbances such as selective logging and fires) alters forest structure and function and influences the forest's carbon sink. In this study, we explored structure-function relationships across a variety of degradation levels in the southern Brazilian Amazon by 1) investigating how forest structural properties vary as a function of degradation history using airborne lidar data; 2) assessing the effects of degradation on solar-induced chlorophyll fluorescence (SIF) seasonality using TROPOMI data; and 3) quantifying the contribution of structural variables to SIF using multiple regression models with stepwise selection of lidar metrics. Forest degradation history was obtained through Landsat time-series classification. We found that fire, logging, and time since disturbance were major determinants of forest structure, and that forests affected by fires experienced larger variability in leaf area index (LAI), canopy height and vertical structure relative to logged and intact forests. Moreover, only recently burned forests showed significantly depressed SIF during the dry season compared to intact forests. Canopy height and the vertical distribution of foliage were the best predictors of SIF. Unexpectedly, we found that wet-season SIF was higher in active regenerating forests (~ 4 years after fires or logging) compared with intact forests, despite lower LAI. Our findings help to elucidate the mechanisms of carbon accumulation in anthropogenically disturbed tropical forests and indicate that they can capture large amounts of carbon while recovering.

Keywords: Amazon, forest degradation, selective logging, forest fires, forest structure, solar-induced chlorophyll fluorescence

1. Introduction

Forest degradation by selective logging, fires and fragmentation affects large regions of the tropics (Bullock et al. 2020; Souza Jr et al. 2013; Tyukavina et al. 2017). In the Amazon region, the drivers of forest degradation are part of a complex socio-economic system that includes forest clearing for pastures and crops, usually preceded by the selective extraction of marketable wood (Broadbent et al. 2008; Lima et al. 2012; Moran 1993). Fire is used extensively for forest clearing and the maintenance of pastures (Aragão et al. 2014; Cochrane 2003). Fires frequently penetrate managed and unmanaged forests so that within the Amazon annually region large areas of forest burn, especially during drought years (Morton et al. 2013).

Forest degradation leads to changes in forest composition, carbon stocks, and forest functions. Logging, fragmentation, and fires promote crown damage and tree mortality resulting in persistent alterations to gap-phase dynamics, potentially leading to species composition shifts toward early-successional, light-demanding species over time (Ordway and Asner 2020). Carbon stocks in degraded forests are highly variable at the local scale, with lightly disturbed forests (e.g., reduced-impact logging) storing as much carbon as intact forests, while forests impacted by multiple fires may lose most of their original carbon stocks (Berenguer et al. 2014; Longo et al. 2016; Rappaport et al. 2018; Silva et al. 2018). Productivity may decline when forests are damaged but may even exceed old-growth forest productivity when forests do not experience further disturbances (Odum 1969). Shifts in degraded forest productivity are driven by changes to forest structure and species composition resulting from increased plant community turnover, disrupted seedling recruitment patterns, and altered nutrient cycling (Bomfim et al. 2020; Dantas de Paula et al. 2015; Prestes et al. 2020; Silva et al. 2018). Water cycling can also be affected by forest degradation. Brief disturbance in evapotranspiration (ET) has been measured in selectively logged forest (Miller et al., 2011). In contrast, ET declined significantly for 3 years after fires and took 7-8 years to recover fully, according to flux tower estimates from the Southern Amazon (Brando et al. 2019).

Forest degradation has also been recognized as a major driver of forest structure changes worldwide. In tropical forests, forest degradation affects live and dead biomass distribution (Longo et al. 2016; Rappaport et al. 2018; Scaranello et al. 2019), the vertical distribution of foliage (Brando et al. 2019; Rangel Pinagé et al. 2019), and canopy gap distribution (Rangel Pinagé et al. 2019; Vaughn et al. 2015). Lidar data can capture both the vertical and horizontal dimensions of forest structure (Drake et al. 2002; Lefsky et al. 2002), hence, it offers an excellent tool to investigate structural changes from degradation processes such as selective logging and fires.

Multilayered, heterogeneously arranged canopies contain a complement of sun and shade leaves functioning optimally under a range of light conditions (Gough et al. 2019). Within temperate intact forests, widespread positive relationships between canopy structural complexity and production were found, suggesting underlying mechanisms of improved canopy light absorption and light-use efficiency (Atkins et al. 2018; Gough et al. 2019; Hardiman et al. 2011). In the Amazon, recent studies have suggested an important role of canopy structural arrangement on phenology (Smith et al. 2019; Tang and Dubayah 2017), but how canopy structural complexity affects the functioning of tropical forests is still a largely uncharted territory. Forest degradation can both enhance or reduce structural complexity (e.g., gaps caused by the removal of large canopy trees increase canopy height variability, or on the other hand, intensive forest fires cause widespread tree mortality and stimulate the regrowth of a uniform understory). Further investigation is needed to clarify the structure-function linkages controlling forest productivity, especially considering the high diversity of species, functional and forest types, as well as disturbance and recovery pathways of tropical forests.

Solar-induced chlorophyll fluorescence (SIF), the natural emission of photons from the light-harvesting structures of plants (Zuromski et al. 2018), is a biophysical consequence of light absorption. SIF may show linear (Sun et al. 2018) or non-linear (Kim et al. 2021) correlation to photosynthesis, depending on many factors such as vegetation type, light regime, averaging period of observations, and plant physiological status. Empirical evidence suggests that SIF is sensitive to canopy properties such as chlorophyll content, leaf area index (LAI) and leaf angle distributions (Koffi et al. 2015; Verrelst et al. 2015). SIF also reflects dynamic photosynthetic responses to heat and water stress (Parazoo et al. 2014).

Until recently, estimation of vegetation productivity from space depended on estimates based on vegetation near-infrared reflectance. SIF appears promising as a physiologically meaningful proxy to photosynthesis at the canopy scale and may be able to capture differences in photosynthesis between intact forests and forests regenerating from anthropogenic or natural disturbances. Another key advantage of SIF is that it is not as much affected by atmospheric scattering due to aerosols and cloud cover (Sun et al. 2018) as traditional vegetation indices such as the Normalized Difference Vegetation Index (NDVI, Rouse Jr et al. 1974) and Enhanced Vegetation Index (EVI, Huete et al. 2002), an aspect that gains even more relevance in the tropics. However, there are many complications of interpreting SIF in complex canopies and illumination conditions such as those found in tropical forests. Recent advances in SIF retrieval techniques and satellite sensors such as the Global Ozone Monitoring Experiment–2 (GOME-2), the Orbiting Carbon Observatory-2 (OCO-2) and the TROPOspheric Monitoring Instrument (TROPOMI) have enabled remote sensing of SIF in unprecedented spatial and temporal scales (Köhler et al. 2018a). TROPOMI SIF data in particular, despite having a coarse spatial resolution (~5.5 km) in relation to the scale of forest disturbances in the Amazon, have fine temporal resolution that allows tracking rapid vegetation changes.

In this study, we use a novel combination of airborne lidar and spaceborne SIF data to investigate solar-induced fluorescence emissions and forest structure variability in intact and degraded forests, also taking into consideration the time since last disturbance events. We address the following questions: 1) How does forest structure change as a function of disturbance history? 2) How does the disturbance history affect SIF emissions and their seasonal patterns? 3) How are forest structural attributes related to SIF across intact and degraded forests?

2. Materials and methods

2.1 Site description

The study area covers approximately 100,000 km^2 at the southern portion of closed-canopy Amazon forests in the Brazilian state of Mato Grosso (Figure 1) and includes a rectangle around the municipality of Feliz Natal. The area is fairly homogeneous in regard to topography, soil and vegetation (Figure S1 of the Supplemental Material) and is covered mostly by ecotonal broadleaf seasonal forests and agricultural/ pastoral managed lands originally covered by forests (IBGE 2021; MapBiomas Project 2019). A five-month dry season (May to September) accounts for only 6% of mean annual precipitation (Figure 1C), and contributes to the extent, duration, and severity of understory forest fires in the study region (Alencar et al. 2015; Morton et al. 2013). Decades of intense land use dynamics have left a mosaic of fragmented and degraded forests in the area, with the majority of intact forests remaining inside the indigenous reserves (Matricardi et al. 2010; Rappaport et al. 2018) (Figure 1B).

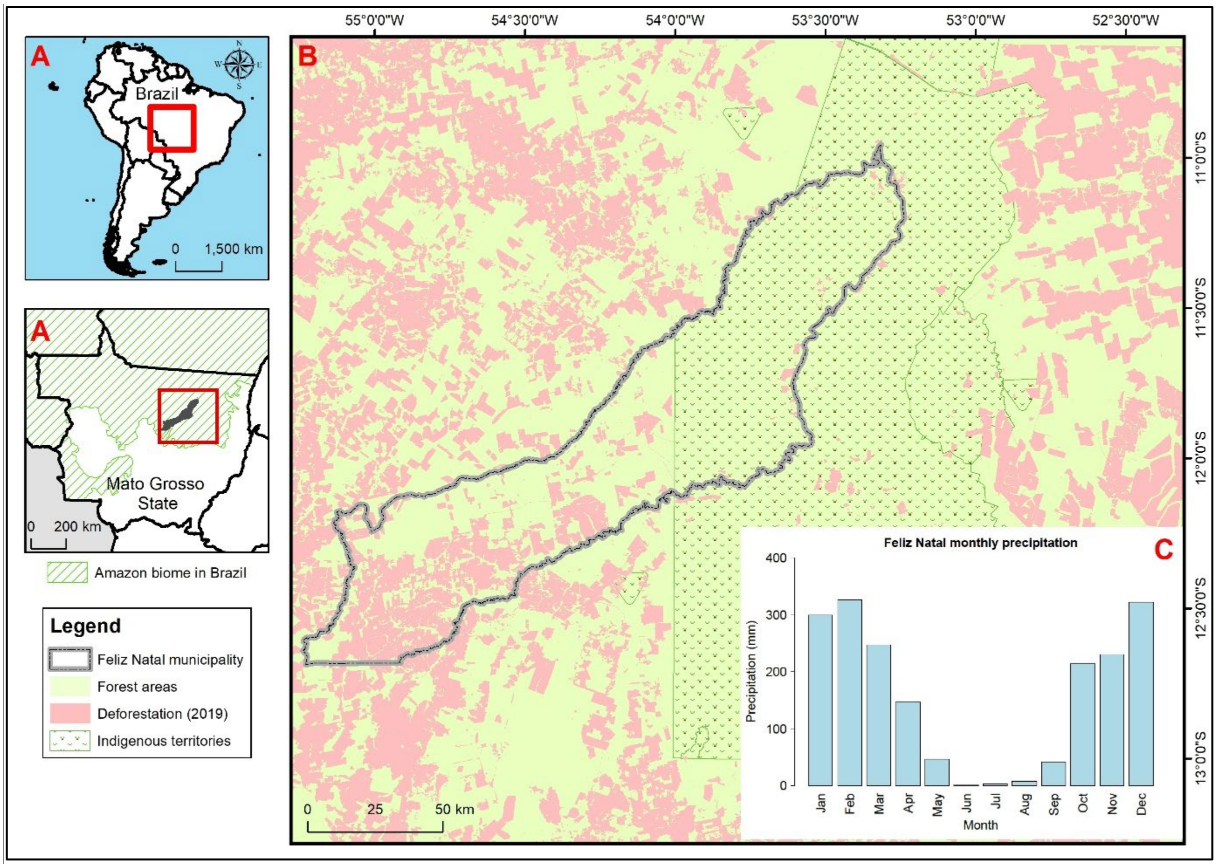

Figure 1. Location (A), land cover (B, INPE 2020) and monthly precipitation (C) of the study area. Source of precipitation data: climate-data.org.

2.2 Remote sensing data

This study leveraged a unique combination of lidar data, TROPOMI observations and land-use history information to investigate forest structure and SIF across a chronosequence of differently aged sites using a variety of remote sensing data. Airborne lidar was used to characterize forest structure, TROPOMI SIF data was used to characterize SIF seasonality, and land use history was classified with a time-series of Landsat observations. Figure 2 provides a graphical overview of the major data sources and analysis steps, whereas each data type is described in a sub-section below.

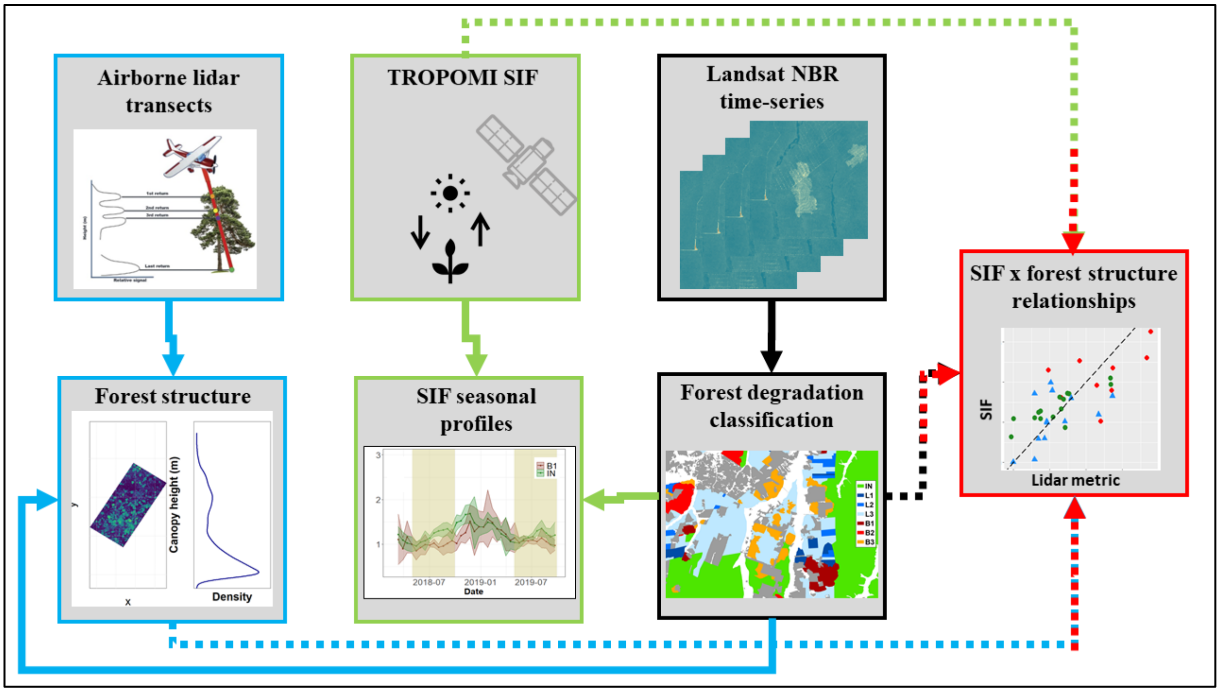

Figure 2. Overview of the major analysis steps and data sources. Blue boxes and arrows refer to forest structure, green boxes and arrows refer to SIF, black boxes and arrows refer to the disturbance history classification, and red boxes and arrows refer to the integrative analysis of structure and SIF.

2.2.1 Airborne lidar data

The airborne, small footprint lidar data employed in this study were drawn from two projects that provide lidar databases for research purposes: Sustainable Landscapes (SL) Brazil (dos-Santos et al. 2019) and Estimativa de Biomassa na Amazônia (EBA, "Biomass Estimates in the Amazon"). We combined these two complementary datasets to increase sample size over our study area: The SL sampling was designed to cover a range of degraded forests, whereas EBA adopted a randomized sampling design that included sampling over intact forests. The acquisition characteristics differ between the two datasets (Table 1), so we thinned SL data to achieve equal return density. Because EBA data were collected in 2016 and the SL data were collected in 2018, we only used intact forest transects from EBA, and assumed the structure of these forests did not change substantially between 2016 (EBA collection year) and 2018 (focal year of the study).

Table 1. Characteristics of the lidar data acquisitions.

Characteristic	SL data	EBA data
Equipment	Optech ORION M300	Riegl LMS Q680i
Acquisition dates	April, 2018	Feb/Apr/Jun, 2016
Flight maximum height	850 m	494 m
Maximum field of view	15°	15°
Scanning frequency	40 KHz	300 KHz
Mean return density per transect	24.89-41.51 points m^{-2}	5.51-6.88 points m^{-2}
Mean first return density per transect	22.59- 33.02 points m^{-2}	4.53-5.18 points m^{-2}
Return density after thinning	5 points m^{-2}	5 points m^{-2}
Original transect size	5 km x 200 m	12.5 km x 300 m
Percentage of flight line overlap	65%	0%

The raw point clouds were pre-processed using the FUSION software (McGaughey 2015) with the following steps: ground points filtering; creation of the terrain surface model at 1-meter resolution from the ground points; point clouds normalization to remove terrain height and get actual height above the ground; standardization of the return density of the point clouds to 5 points per square meter (EBA data average density); creation of the canopy height models from the normalized point clouds; and clipping of the point clouds to the spatial extent of the lidar transects classified according to the disturbance classes.

To estimate structural parameters across our disturbance classes (the disturbance history classification is described in section 2.2.3), we computed a set of lidar-derived metrics from the normalized, standardized point clouds. The first set of calculated metrics was the vertical distribution of Leaf Area Densities (LAD) and total Leaf Area Index (LAI). We estimated the average LAD by layers using the method proposed by MacArthur and Horn (1969) to estimate foliage-height profiles, following the equation:

$$LAD_{i-1,\ i} = \ln\left(\frac{S_e}{S_t}\right)\frac{1}{k\Delta z}$$

where for each vertical column of voxels, i is a voxel in a sequentially ordered vertical column of the canopy, S_e is the number of pulses entering the given voxel, S_t is the number of pulses exiting the same voxel, k is an extinction coefficient, and z represents the height of a voxel. The term k represents a Beer-Lambert Law extinction coefficient, which describes the attenuation of radiation by a medium or an object. When applied to forest canopies, this coefficient includes a correction for the non-random distribution and orientation of the foliage and the thickness of the leaf material and the forest canopy. We followed Stark et al. (2012) and used k = 0.5 (i.e., assumed no clumping and random orientation of leaves). The voxel's horizontal resolution was defined as 30 meters and vertical resolution (or the canopy layer thickness), as 1 meter. Total LAI was calculated as the vertical integral of the LAD profile. LAD below 4.5 m height were excluded from LAI calculations because LAD estimates are unreliable at lower heights. As the canopy becomes denser and more leaves are encountered, the penetration of lidar pulses diminishes, causing sample sizes for estimating LAD to decrease and error to increase (Kamoske et al. 2019). LAD profiles and total LAI were estimated using the *leafR* package (Almeida et al. 2019).

To model structure-SIF relationships, we calculated canopy height and other types of metrics to be included as predictors of SIF (Table 2). These metrics were calculated using all the points in the lidar point cloud (i.e., first, second, third and fourth returns were all considered) that are above the specified height cut-off value (1.5 m), at 100 m grid cell size, to fit within the maximum 200 m width of the SL lidar transects. We examined 23 metrics and categorized them into four broad structural aspects: canopy height, foliar distribution, horizontal complexity and vertical complexity (Table 2). Canopy height metrics measure the distribution of lidar returns in the vertical dimension, with specific sensitivity to canopy openness and roughness at different heights of the forest vertical profile (Falkowski et al. 2009). Foliar distribution influences light transmittance and absorbance, and therefore, exerts large control on photosynthesis. Horizontal complexity metrics are based on the canopy height model (CHM), while vertical complexity is described using the vertical foliage profile (VFP). CHM-based metrics describe the heterogeneity of the canopy surface, including ground pixels, i.e., canopy gaps. VFP-based metrics describe the vertical layering of the reconstructed foliage profile, and weights profile parts in the lower heights to compensate for the occlusion by high trees (Knapp et al. 2020). It is important to note that this structural categorization was adopted for the construction of the models, but the metrics can be related to more than one structural aspect. The metrics used as SIF predictors were computed using the *lidR* package (Roussel et al. 2020) in the R statistical environment (R Core Team 2019).

Table 2. Lidar-derived metrics included as predictors of SIF.

Metric	Description	Structural aspect	Citation
Mean	Average of return heights mean within the grid cells	Canopy height	
Sd	Average standard deviation of return heights within the grid cells	Canopy height	
Skew	Average skewness of return heights within the grid cells	Canopy height	
Kurt	Average kurtosis of return heights within the grid cells	Canopy height	
P10	Average 10th percentile of return heights within the grid cells	Canopy height	
sdP10	Standard deviation of 10th percentile of return heights within the grid cells	Canopy height	
P25	Average 25th percentile of return heights within the grid cells; in the study area, it is an indicator of understory density.	Canopy height	
sdP25	Standard deviation of 25th percentile of return heights within the grid cells	Canopy height	

P50	Average 50th percentile of return heights within the grid cells	Canopy height	
sdP50	Standard deviation of 50th percentile of return heights within the grid cells	Canopy height	
P75	Average 75th percentile of return heights within the grid cells	Canopy height	
sdP75	Standard deviation of 75th percentile of return heights within the grid cells	Canopy height	
P95	Average 95th percentile of return heights within the grid cells; it represents an unbiased measure of top of canopy height	Canopy height	
sdP95	Standard deviation of 95th percentile of return heights within the grid cells	Canopy height	
LAI	Total leaf area index (LAI) above 4.5m	Foliar distribution	
f_sun	Fraction of sunlit leaves, estimated as exp (-k * LAI), where k is the coefficient of light extinction	Foliar distribution	Clark et al. (2011)
sdVFP	Standard deviation of vertical foliage profile	Foliar distribution	
cvVFP	Coefficient of variation of vertical foliage profile	Foliar distribution	
Rumple	Rumple Index, which indicates the roughness of a surface. It is calculated as the ratio between its area and its projected area on the ground.	Horizontal complexity	(Kane et al. 2010; Parker and Russ 2004)
CRR	Canopy relief ratio, a quantitative descriptor of the relative shape of the canopy defined as (mean height–min height) / (max height–min height)	Horizontal complexity	Parker and Russ (2004)
Gini	Gini coefficient of foliage structural diversity	Vertical complexity	Valbuena et al. (2017)
Shannon	Shannon index, applied to quantify the diversity and the evenness of the vertical distribution of return heights.	Vertical complexity	Stark et al. (2012)
VCI	A fixed normalization of the Shannon Index	Vertical complexity	van Ewijk et al. (2011)

2.2.2 Solar-induced chlorophyll fluorescence (SIF) data

We used ungridded TROPOMI instantaneous SIF data resampled to a 0.05° x 0.05° spatial resolution (Köhler et al. 2018a). This dataset is available from November/2017 until the present. TROPOMI has a wide swath of 2,600 km with daily, near-global coverage, with a 16-days revisit cycle. The phase angle (the angle between the axes from the sounding to the sun and to TROPOMI's sensor) of each sounding varies along the swath. A study from Doughty et al. (2019) showed that, with a sufficient number of observations from different angles, the effect of phase angle of observations in SIF seasonal patterns in the Amazon is negligible, hence, we used all available SIF data, regardless of sun-sensor geometries. SIF retrievals from 18 months from March 2018 to September 2019 were selected before the abnormally active fire season in 2019 (Brando et al. 2020). TROPOMI observations are pre-filtered to remove soundings that are affected by high radiance levels due to cloud albedo and that have > 80% of cloud fraction (Köhler et al. 2018a), as SIF cannot be detected with heavily thick clouds (Frankenberg et al. 2012). We acknowledge a potential effect of clouds on SIF seasonality, but since our focus is to compare SIF behaviour across disturbance classes, we adopted a less strict cloud filter to maximize the number of observations during the wet season.

We employed a multi-step approach to extract SIF seasonal estimates for each disturbance class. As most of the forest degradation polygons were smaller than one TROPOMI footprint, we calculated the area proportion for each disturbance class in the resampled grid cell, and after examining the sample size resulting from a few thresholds (e.g., 100%, 90%, 80%), only included in the analysis those cells covered by at least 70% of any class. This approach aimed to minimize pixel mixtures and was adopted as a compromise between pursuing a pure spectral SIF signal and a sufficient sample size. Nonetheless, it resulted in an unbalanced sample size among classes (refer to last column of Table 4). Therefore, we took four steps to facilitate comparisons across classes: a) computation of daily median values across all cells of each disturbance class; b) interpolation of missing data using linear interpolation; c) smoothing the daily data using Savitzky-Golay (SG) filter (Savitzky and Golay 1964), to minimize noise in SIF data; and d) averaging daily data to 16 days (TROPOMI's revisit interval).

2.2.3 Disturbance history classification

To characterize the disturbance history of our study area (2000–2019), we masked out deforested areas using deforestation data until 2019 (INPE 2020). Subsequently, forest degradation (logging and fires) on the forest remnants was mapped based on a time-series of Landsat images. Intact, logged and burned areas were visually identified based on their spatial patterns (Figure S2) and classified into seven disturbance classes: intact forests (IN), 0-3 years (L1), 4-7 years (L2), and 8-14 (L3) years after logging, and 0-3 years (B1), 4-7 years (B2), and 8-14 (B3) years after burning. Details of the disturbance history classification are described in the section 2 of the Supplemental Material.

Lidar transects were classified into one of the disturbance classes based on the Landsat disturbance history. To prevent mixed classes, original transects overlapping more than one class were split accordingly. Transects cut by established roads were also split to exclude the road portions (even if they covered the same class), and a 100 m buffer was applied in the transect area to minimize edge effects caused by roads in the lidar estimates. We used the Canopy Height Model (CHM) of each transect to visually confirm their degradation status in 2018 and adjusted when necessary. For instance, in the CHM of recently logged forests, one can see roads and canopy gaps, and in the CHM of burned forests, one can identify a lower and more homogeneous canopy. As shown in Table 3, every disturbance class considered in this study had at least 30 ha of forests surveyed by lidar.

Table 3. Disturbance classes of the lidar samples.

Disturbance class	**Number of transects**	**Mean area (ha)**
Intact (IN)	22	162.1
0-3 years after logging (L1)	6	34.49
4-7 years after logging (L2)	14	71.20
8-14 years after logging (L3)	16	72.97
0-3 years after fires (B1)	8	45.95
4-7 years after fires (B2)	9	74.28
8-14 years after fires (B3)	10	58.41
Total	85	

The classification of disturbance classes for SIF data involved areas beyond the lidar transects, since SIF data is available for the entire study area. In addition to the deforested areas, we also masked out pioneer vegetation which occupies vast extensions of the Xingu River floodplains (RADAMBRASIL 1983), as these areas present spectral properties similar to burned forests. Subsequently, the remaining polygons were split when needed and classified into one of the disturbance classes, which included intact forests as the control, undisturbed class. Due to the large footprint of TROPOMI data, we eliminated isolated polygons with area smaller than 50 hectares and merged contiguous polygons within this same area threshold to the largest neighboring polygon. Polygons that experienced multiple degradation events during the time-series were classified according to the latest event, and polygons completely surrounded by deforested areas (i.e., in the edges of the study area) were not included in the samples. Some of the disturbance classes had very few polygons, resulting in uneven sample size among classes (Table 4).

Table 4. Characteristics of SIF samples.

Disturbance class	# of polygons	Mean area (ha)	# of TROPOMI cells (70%)	# of TROPOMI cells (100%)
Intact (IN)	85	28,343	611	366
0-3 years after logging (L1)	118	1,481	7	1
4-7 years after logging (L2)	94	1,377	4	0
8-14 years after logging (L3)	145	107,759	250	32
0-3 years after fires (B1)	162	3,844	81	13
4-7 years after fires (B2)	74	1,845	9	0
8-14 years after fires (B3)	270	2,124	51	4
Total	934			

2.3 Modelling forest structure and SIF relationships

To model forest structure-SIF relationships, we obtained paired lidar-SIF observations by analysing the land-use context of each lidar transect and surrounding areas and selecting homogeneous SIF grid cells overlapping lidar transects, based on the assumption that the selected transects are representative for the conditions of the entire SIF footprint. Because relatively few lidar transects are available, and land use mixtures within the SIF footprint are common, we could not find samples of every disturbance class (Table 4). Instead, we aggregated classes broadly into three groups (intact, logged and burned forests) discounting time since disturbance. Footprints with mixed logged and burned areas in their disturbance history were not included. The lidar coverage area in each SIF cell varied. Figure 3 shows examples of intact, logged and burned forest samples and the available sample size for each class.

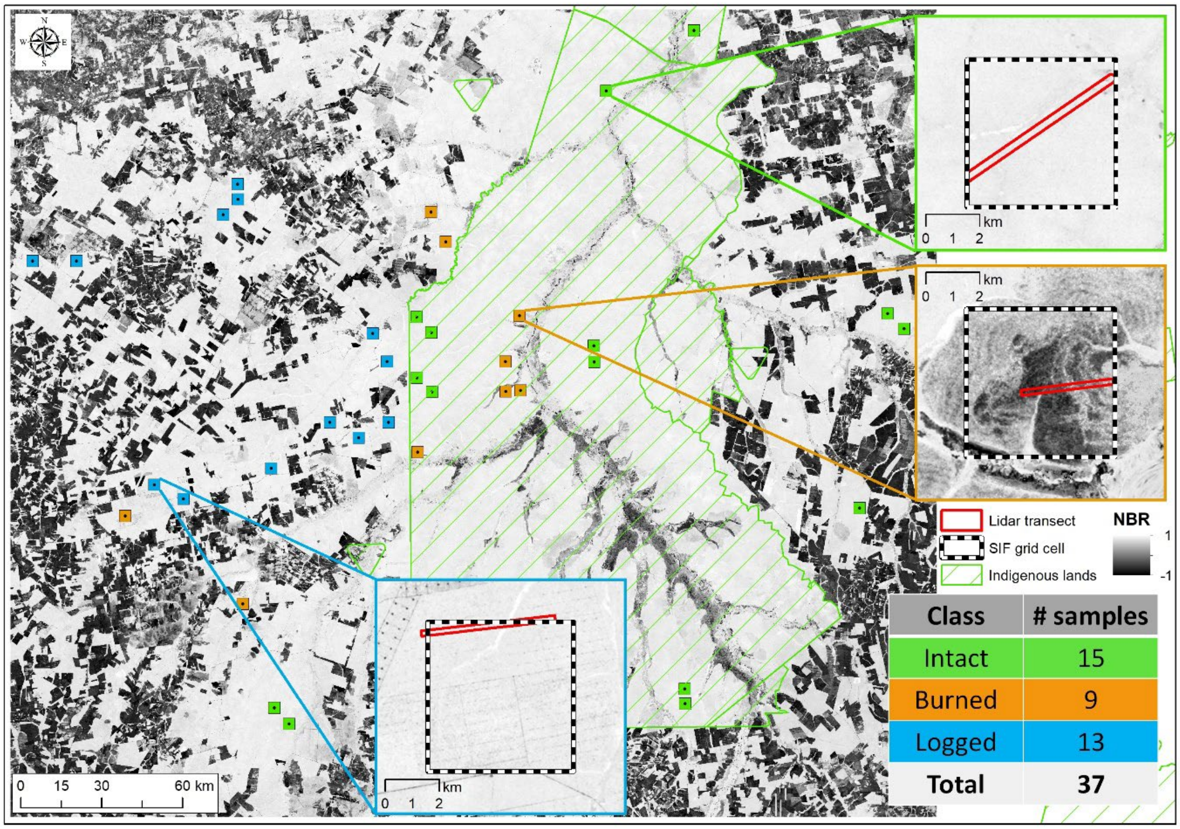

Figure 3. Example of SIF grid cell selection (intact at green, logged at blue and burned forests at orange inset) according to pixel mixture and availability of lidar transect. Background images are NBR annual composites from 2019 (main map and intact forest inset), 2016 (logged forest inset) and 2010 (burned forest inset). Lighter areas in the NBR image represent dense canopy cover, while darker areas represent low or no canopy cover. Degradation by fire or logging appears in intermediate grey tones.

The response of SIF varies on short time scales and seasonally, in contrast to forest structure measured by lidar that varies on multi-annual time scales. Therefore, we chose to aggregate SIF in our investigation of the relation of SIF to forest structure. Through our data exploration, we noticed that SIF retrievals during the dry season were more stable, likely due to the large number of available observations so that the average is more robust. We extracted the daily SIF values for each of the 37-cell samples and calculated the median of those values across the months of April 2018 through June 2018. The SL lidar data was acquired nearly simultaneously in April 2018.

2.4 Statistical analysis

To test for differences in LAI among the disturbance classes, we tested the LAI data for the normality assumption using the Shapiro-Wilk test, which indicated that although the entire sample does not follow a normal distribution, the LAI for all the individual disturbance classes met the assumption (p-value > 0.05). Hence, we performed a multiple pairwise t-test to compare the means of disturbed classes against the mean of intact forests and reported statistical significance. To statistically compare the SIF seasonal profiles of intact and disturbed forests, we plotted the SIF spatio-temporal averages (spatial aggregation of the 0.05° x 0.05° grid cells covered with >70% by a given disturbance class over the 16-days window), along with their 95% confidence interval. In addition, we paired the 16-days averaged SIF data of intact and each degraded forest class (so that each pair represents SIF from the same time but different disturbance class/location) and ran linear regression models using these pairs for the wet and dry periods separately, to assess how SIF from degraded forests compared to SIF from intact forests seasonally.

To estimate the contribution of lidar-derived structural variables to SIF variability, we developed a linear regression model for each structural aspect (e.g., canopy height, foliar distribution, horizontal complexity, and vertical complexity). We used stepwise selection to identify the simplest and yet most informative combination of variables (Miller 1984). This selection method performs multiple iterations by dropping one predictor variable at a time. The Akaike information criterion (AIC) of the models is computed and the model that yields the lowest AIC is retained for the next iteration. Given a collection of models for the data, AIC estimates the quality of each model relative to other possible models, and thus, it provides a means for model selection (Aho et al. 2014). To address multicollinearity, we excluded highly correlated variables ($r \geq 0.80$) before model selection and confirmed that each predictor in the final models showed the variance inflation factor (VIF) less than 10. We also fitted regression models with the structural predictors as fixed effects and disturbance condition (intact, logged or burned) as conditional effects to test for the presence of interaction between disturbance condition and the lidar metrics while predicting SIF from structural attributes. Finally, we compared the two pairs of models (with and without interaction) using Analysis of Variance. Functions *stepAIC, vif* and *anova* from *MASS* (Venables and Ripley 2002), *car* (Fox and Weisberg 2019) and *stats* packages were used to perform these steps. All statistical tests, analysis and plotting were performed in the R statistical environment (R Core Team 2019).

3. Results

3.1 Structural properties of intact and degraded forests

The structural properties of degraded forests, estimated using high-density airborne lidar data, demonstrated greater changes for burned versus logged areas, compared to intact forests (an example showing eight-hectare samples for each disturbance class is presented in Figure 4). The most obvious effect of disturbance on forest structure is the decrease of canopy heights of the disturbance classes, as depicted by the examples in Figure 4.

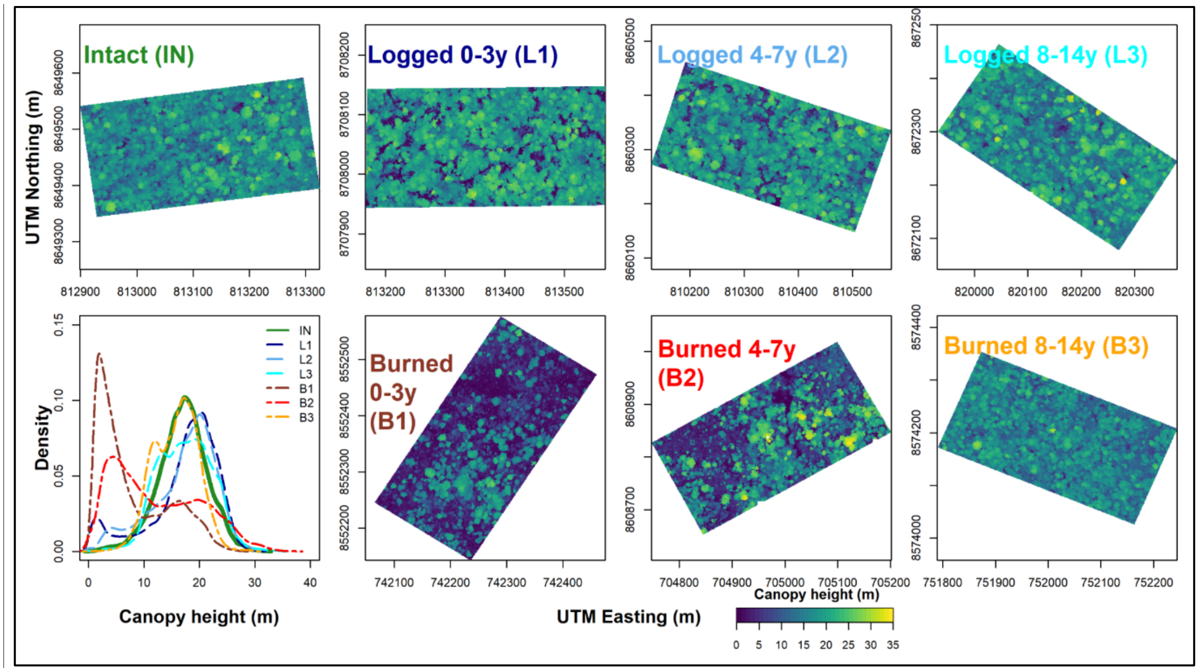

Figure 4. Lidar-derived canopy height models and associated density plots of 8-ha sample plots for each disturbance class.

Logging was associated with a greater frequency of canopy gaps (height < 7 m), but not overall shorter canopies (Figure 4). Burned areas, especially from B1 and B2 classes, showed significant decreases in canopy height (with height modes of ~5m, compared to ~20m of logged and intact forests) and changes in height distributions from unimodal to bimodal due to mortality of tall trees and subsequent understory development (Figure 4 and Figure 5). Additional height metrics that describe the vertical structure of the forests (such as height percentiles) were also affected by disturbance (Figure S3): time since disturbance had a negative effect on lower and mid-canopy (10^{th} to 75^{th} percentiles) of burned forests but not at the top-of-the canopy (95^{th} percentile), where B2 class showed lower values than B1. Logged forests did not show consistency in height percentiles with time since disturbance. Overall, both logging and fire disturbances introduced more variability in the height metrics (Figure S3).

Leaf area density of forests in Feliz Natal region decreased with height (Figure 5A). Overall, the vertical foliage profile of logged forests showed the same shape of intact forests' profiles. Forests logged 0 to 7 years prior to lidar acquisition showed greater leaf area density (LAD) in the understory (up to ~ 7m) and lower LAD in the mid-canopy (up to ~ 20 m). The older logging class overlapped intact forests in much of the vertical profile, with slightly higher leaf area density at heights above 20 meters. Transects of intact and older logged forests also presented similar LAI distributions (Figure 5B).

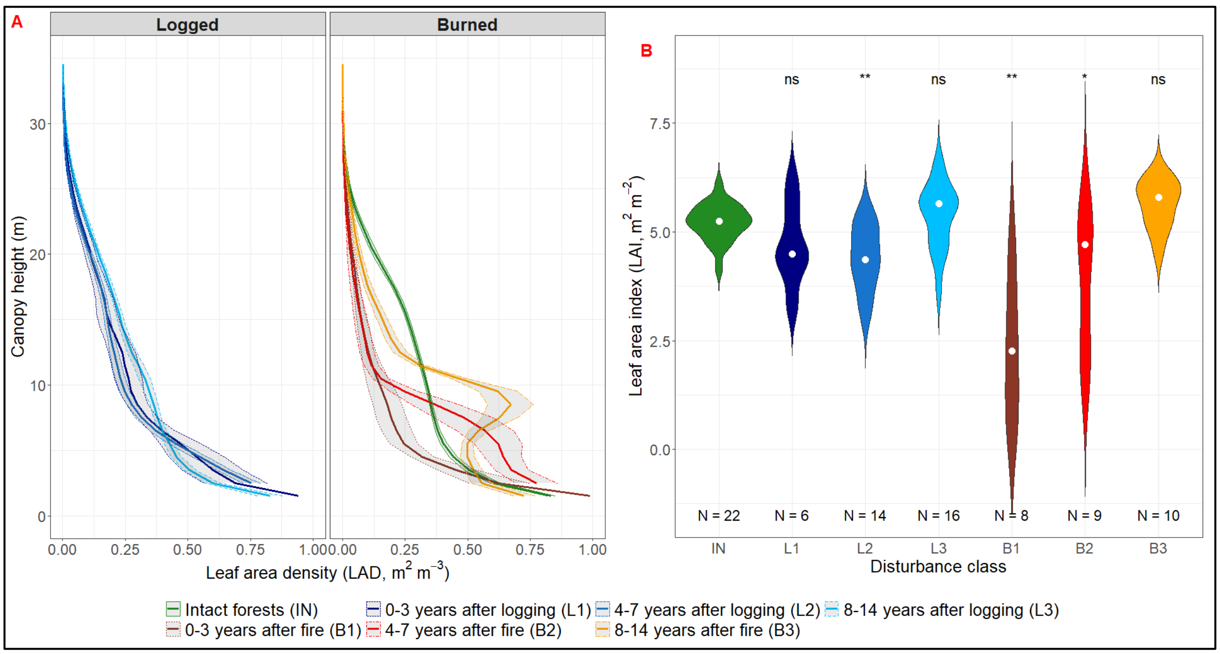

Figure 5. Panel A: Vertical foliage profile for the disturbance classes. Intact forest's LAD is plotted over logged and burned forests' plots as a reference. Bands along the lines represent the standard error. Panel B: Distribution of leaf area index (LAI) above 4.5m for the disturbance classes. The violin plots summarize LAI distributions as a function of disturbance class and show the kernel probability density of the data at different values. All violins have the same area. The median of each group is indicated by the white dots. The symbols on the top indicate statistical significance (p-values, ns = $p > 0.05$; * = $p \leq 0.05$; ** $p \leq 0.01$) as computed from the multiple pairwise test against a reference group (IN, intact forests).

Burned forests showed large vertical variation according to the time since disturbance, and none of the burned profiles resembled intact forests' profile (Figure 5A). Forest burned in the last 7 years showed the foliage peaks in the understory (0.75 and 0.6 m^2 m^{-3} at 3 and 7 m for B1 and B2 classes, respectively), and even the oldest burned class (B3) showed lower foliage density (0.12 m^2 m^{-3}) in the mid- to upper canopy layers (> 15m) than intact forests (0.25 m^2 m^{-3}). The profiles of burned forests clearly showed the canopy increasing in height over time. Patterns of light transmission and absorption through the forest canopy, which are strongly influenced by vertical leaf area distribution, were also impacted by fires and logging: light transmittance was similar among intact and logged classes, except for higher levels of light reaching the understory of the more recent classes, whereas burned forests exhibited different patterns of light transmittance according to times since disturbance, attaining greater levels of light at lower depths in the canopy (Figure S4A). Absorption of light had a strong peak around 18m height for intact and logged forests, whereas areas B1 peaked at ~4m height, B2 peaked at ~8m, and B3 peaked at ~10m height (Figure S4B).

The total LAI varied dramatically among disturbance classes (Figure 5B), ranging from 0.5 to 6.5 m^2 m^{-2}. Burned transects demonstrated consistent LAI recovery with time since disturbance, with differences between burned and intact forests diminishing with time since fire. On the other hand, logged areas showed higher LAI than burned forests with L1 and L3 not differing significantly from intact forests. Even though not significant, L1 still tended to have lower LAI than intact forests. Taken along with the results for L2, this implies a small but consistent reduction in LAI with logging even after 7 years of recovery.

3.2 SIF at intact and degraded forests

Seasonal SIF as estimated by TROPOMI observations revealed limited SIF differences among disturbance classes. The time-series of SIF data showed seasonality, with SIF increasing towards the end of the dry season (months with precipitation < 100mm) and peaking in the early wet season, with a two-fold increase in intact forests signal. Regarding the disturbance classes, B1 markedly differed from intact forests, with lower values in the end of the dry season (Figure 6A), whereas B2 showed higher averages than intact forests after the SIF peak, despite overlapping confidence intervals (Figure 6B). The other classes seemed to follow the same seasonal pattern (Figure 6C-F) as intact forests, however, the latter showed a more stable signal, while L1, L2 and B2 classes showed large variability in the estimates of the 16-days SIF averages, likely due to the low sample size.

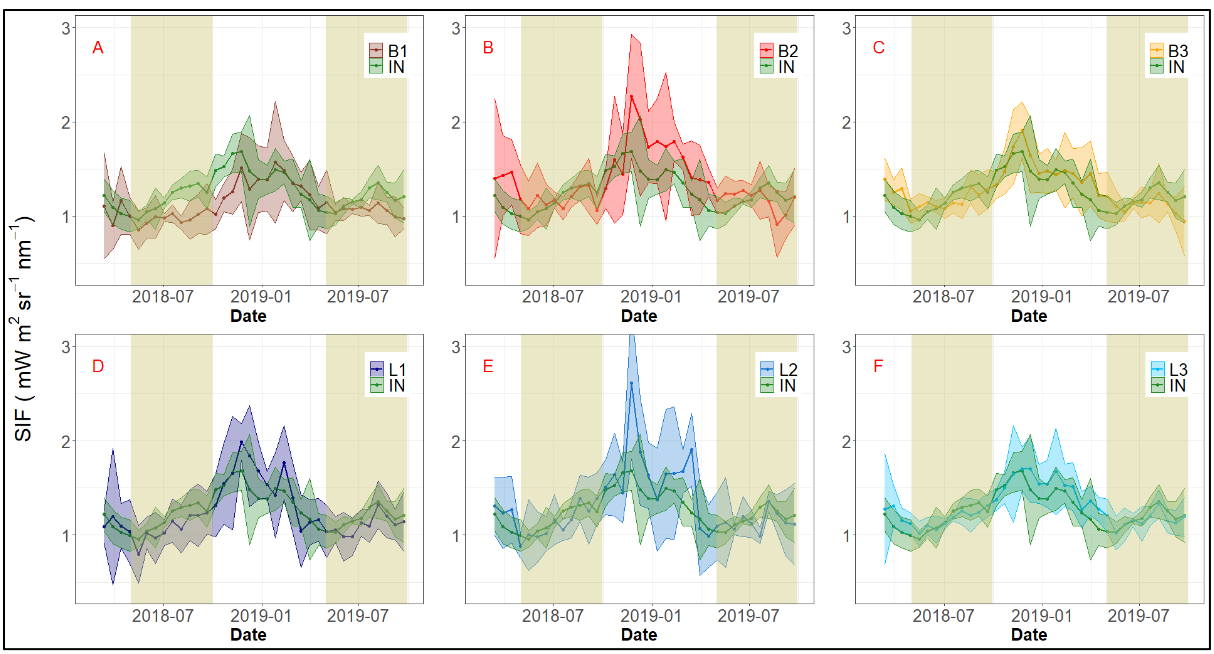

Figure 6. SIF time-series (daily data averaged to 16-days) for the disturbed classes with intact forests time-series as reference. The included period is March 1st, 2018, to September 30th, 2019. Beige shades indicate the dry season (months with <100mm precipitation) in the study area. Lines represent the median value of the 16-days average. The bands represent the 95% confidence interval for the median and provide an indication of whether the estimates of SIF

for intact and disturbed forests overlap. Disturbance classes are intact forests (IN), 0-3 years (B1), 4-7 years (B2), and 8-14 (B3) years after fires, and 0-3 years (L1), 4-7 years (L2), and 8-14 (L3) years after logging.

Given the notable seasonality of SIF, we also compared SIF values for the dry and the wet season months, by pairing 16-day averages of disturbed classes to intact forests' 16-day averages (Figure 7). A general pattern is that in the wet period, SIF from disturbed classes was more correlated with and usually higher than intact forest's SIF. In the dry season, intact forests have mostly higher SIF than disturbed forests, with the most severely disturbed classes (e.g., B1 and B2) showing much lower SIF. Across all classes and seasons, the older disturbance classes (L3 and B3) showed the best agreement with intact forests (R^2 of 0.93 and 0.90, respectively). We also found a consistent pattern of SIF from disturbed classes being slightly lower than intact forest SIF during the dry season and a reversed trend in the wet season, except for B1, that is lower than intact forest in both seasons (Figure 7). Moreover, the regression lines get closer to the 1:1 line with time since disturbance, indicating SIF recovery.

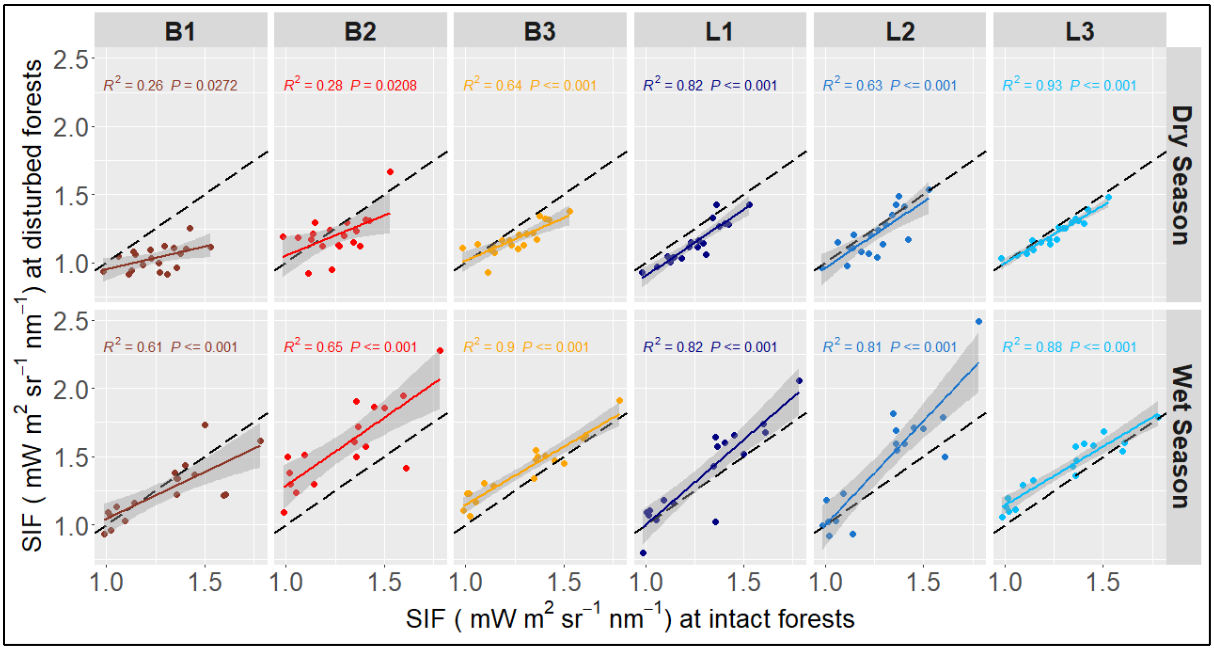

Figure 7. Comparison of averaged SIF values between intact and disturbed forests across wet and dry seasons. Coloured lines represent the best fit, black dashed lines indicate the 1:1 line, and grey bands represent 95% confidence intervals. Disturbance classes are intact forests (IN), 0-3 years (B1), 4-7 years (B2), and 8-14 (B3) years after fires, and 0-3 years (L1), 4-7 years (L2), and 8-14 (L3) years after logging.

3.3 Structural predictors of SIF

Structural variables partially explained SIF variability. The best lidar-based model of SIF included canopy height descriptors (Table 5, Figure 8), with adjusted R^2 of 0.44, p-value <0.05, and RMSE = 0.067 mW m^2 sr^{-1} nm^{-1}. The mean and standard deviation of height, as well as standard deviation of 25th and 95th percentiles were the most important predictors of SIF according to this model. The model based on foliar distribution predictors showed the second-best performance (p-value <0.05, adjusted R^2 of 0.30, RMSE = 0.076). We note that the metric sdVFP, the standard deviation of the vertical foliage profile, was the strongest single predictor variable of SIF, accounting for approximately 22% of SIF variability (model results not shown). The models for horizontal and vertical complexity showed poor performance and non-significant coefficients.

The variance inflation factor (VIF) of the predictors of all models were less than 10, indicating that they provide independent information for SIF predictions.

Table 5. Equations, adjusted R^2 (Adj. R^2), absolute root mean square error (RMSE), and F-statistic p-value of the tested models. The selected metrics are: mean (average of return heights mean within the grid cells); sd (average standard deviation of return heights within the grid cells); sdP25 (standard deviation of 25th percentile of return heights within the grid cells); sdP95 (standard deviation of 95th percentile of return heights within the grid cells); sdVFP (standard deviation of vertical foliage profile); cvVFP (coefficient of variation of vertical foliage profile); LAI: (total leaf area index above 4.5m); Rumple (Rumple index); CRR (canopy relief ratio); Gini: (Gini coefficient of foliage structural diversity); Shannon (Shannon index); VCI (a fixed normalization of the Shannon index). For more details about the metrics, refer to Table 2.

Model	Equation	Adj. R^2	RMSE	Relative RMSE (%)	p-value
Canopy height	SIF = 1.507 + 0.207 * mean - 0.039 * sd - 0.169 * sdP25 - 0.058 * sdP95	0.44	0.067	20.6	0.0001
Foliar distribution	SIF = 0.4609 + 1.1289 * sdVFP + 0.0012 * cvVFP + 0.0538 * LAI	0.3	0.076	31.9	0.0019
Horizontal complexity	SIF = 1.213 - 0.005 * Rumple - 0.227 * CRR	-0.03	0.094	134.1	0.6207
Vertical complexity	SIF = 1.39 + 0.35 * Gini - 0.14 * Shannon - 0.24 * VCI	0.01	0.09	56.7	0.3604

The scatterplots of observed versus predicted values of the selected models confirmed the different performance of the tested models (Figure 8). The correlation between observed and fitted values ranged from 0.71 (best model) to 0.17 (poorest model). An interesting pattern emerged from the visualization of models' results: SIF values of burned forests' samples were usually the highest, while SIF values from intact and logged forests mixed at lower ranges of SIF.

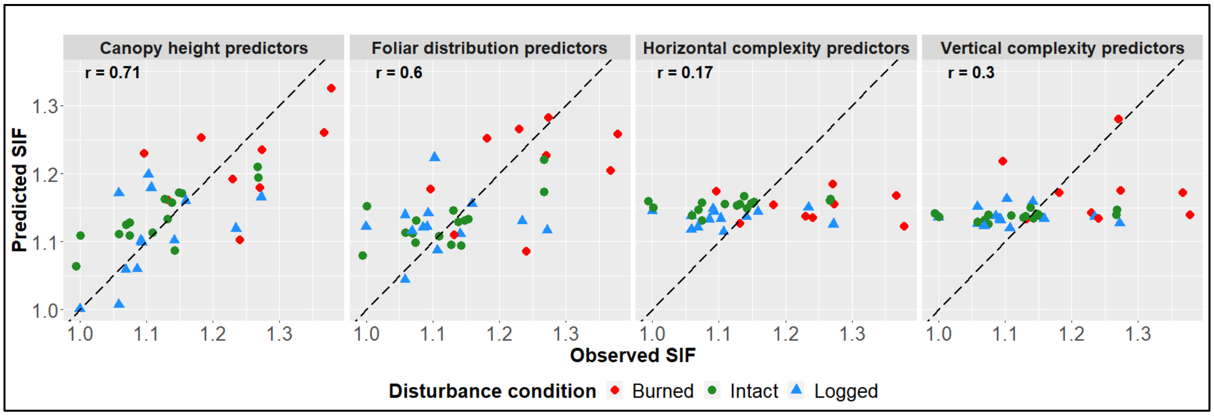

Figure 8. Observed versus predicted values of SIF as estimated by the models. Each dot represents the median value of SIF observations across the months of April-June 2018 and the SIF value predicted from lidar metrics for a given 'pure SIF pixel'. Dashed line is the 1:1 line, and r values represent the Pearson correlation coefficient between observed and predicted values.

We tested for the presence of interaction between disturbance condition and the lidar metrics (in the canopy height and foliar distribution models only) and found that the inclusion of disturbance condition on the models led to improvements in SIF predictions (Table 6), increasing the adjusted R^2 of the canopy height model from 0.44 to 0.47 and of the foliar distribution from 0.30 to 0.33. RMSE from both models also decreased slightly.

Table 6. Equations, adjusted R^2 (Adj. R^2), absolute root mean square error (RMSE), and F-statistic p-value of canopy height and foliar distribution including interactions.

Model	Equation	Adj. R^2	RMSE	Relative RMSE (%)	p-value
Canopy height with interaction	SIF = 1.418 + 0.152 * mean - 0.037 * sd - 0.120 * sdP25 - 0.037 * sdP95 + 0.059 * bdcatLogged + 0.211 * bdcatBurned - 0.016 * sdP95:bdcatLogged - 0.042 * sdP95:bdcatBurned	0.47	0.061	16.6	0.0007
Foliar distribution with interaction	SIF = 0.6623 + 0.3569 * sdVFP + 0.0014 * cvVFP + 0.0326 * LAI - 0.0119 * bdcatLogged - 0.0142 * bdcatBurned + 0.0066 *	0.33	0.07	28.2	0.0075

	LAI:bdcatLogged + 0.0268 * LAI:bdcatBurned

When we compared the two pairs of models (with and without interaction) using Analysis of Variance, the results did not indicate a significant improvement when accounting for the interaction (p-value > 0.2 for both comparisons). These results do not support the inclusion of disturbance class as an independent variable (i.e., disturbance impacts as mediated by structure alone).

4. Discussion

In this study, we used multi-source remote sensing data to assess the effects of tropical forest degradation (fires and selective logging) on canopy structural attributes and SIF. Moreover, we modelled the contribution of lidar-derived structural variables to SIF variability. Our results highlighted disturbance type and recovery time as important drivers of forest structure and SIF. We also showed that forest regeneration can result in higher SIF, presumably due to structural, compositional and physiological changes. Canopy structural properties predicted about 44% of SIF variability, suggesting that canopy structure plays a significant role in mediating photosynthesis in degraded Amazon forests.

4.1 Distinct responses of structure and SIF to disturbance

Despite remarkable differences of structural attributes among intact forests and forests regenerating from degradation (Figure 4, Figure 5, and Figure S3), their SIF seasonal cycles were unexpectedly similar, except for the recently-burned, B1 class. These findings likely indicate optimized resource use by post-disturbance growing (which might include grasses) and fire-resistant vegetation (Berenguer et al. 2018; Brando et al. 2019). However, the rapid (3-6 years) restoration of SIF to pre-disturbance values was not accompanied by restoration of the original forest structure (Figure 5). Spatial and temporal scales should be taken into consideration when interpreting these results. SIF coarse grain size differs substantially from the lidar small footprint, but also does the temporal and spatial variability of forest structural properties and productivity. While forest structure changes slowly and at small scales, forest productivity may change sub-daily and over larger extents.

The absolute height above ground for a given height percentile metric was generally significantly lower in disturbed classes than in intact forests (Figure S3), with burned forests showing larger differences. Forest degradation rearranged the vertical distribution of foliage, and the resulting related patterns of light transmittance were remarkably different in some cases (e.g., in the older burned areas, Figure 5 and Figure S4). Meanwhile, SIF differences among the classes, when analysed at the landscape scale, were minimal and associated with seasonality. We raised some hypotheses to explain SIF seasonal patterns being similar across degradation classes except for the recently burned sites despite the forests being structurally different. First, species turnover is higher in regenerating forests (Villa et al. 2018; Zhang et al. 2008), which would delay recovery of vertical and horizontal structures. Second, SIF signal may saturate rather quickly and may not be able to detect more subtle differences. The SIF signal saturation may be related to canopy structure, shadowing and re-absorption of the SIF radiation in complex canopies, as discussed in the next section. Further research is needed to fully elucidate SIF interactions in complex tropical forest canopies and how canopy structure affects the subtle SIF signal that is sensed by orbital platforms.

4.2 SIF variability related to disturbance

SIF time-series showed a clear seasonal signal (Figure 6), with a peak of photosynthetic activity in the early wet season, a trend similar to that found by Doughty et al. (2019) and Köhler et al. (2018b) for the entire Amazon. This phenomenon, related to the dry-season green-up in the Amazon, has been widely observed and debated (Huete et al. 2006; Köhler et al. 2018b; Tang and Dubayah 2017; Wu et al. 2016). We did not observe specific phenological shifts (e.g., changes in the timing of peak SIF) with disturbance. Instead, we found depressed SIF values on the most recent burned class starting early in the dry season and lasting until the peak at the start of the wet season. The confidence intervals of the recently burned areas mostly did not overlap with those from intact forests during this period, indicating significant SIF differences, likely due to the loss of photosynthetically active material (e.g., reduced LAI, Figure 5).

There was a consistent pattern of SIF from disturbed classes being slightly lower than intact forest SIF during the dry season and a reversed trend in the wet season (Figure 7). This pattern may be due to the highly productive species, typical of early- and mid-stages succession, that must transpire substantially more to support rapid productivity but lack the deep root systems to sustain high ET levels in the dry season (Brum et al. 2019; Nepstad et al. 1994). These results are consistent with model simulations from Longo et al. (2020) which predicted that severely degraded forests (as is the case of our B1 class) experience increased water stress with declines in ET and gross primary productivity during the dry months.

In addition to the mechanisms we proposed to explain the SIF seasonal patterns at degraded forests, other factors could be influencing our results. The complex photosynthetic energy balance is also regulated by air temperature and water availability (Porcar-Castell 2011), thus the higher temperatures and lower water availability in the heavily degraded forests such as our B1 class during the dry season (Longo et al. 2020) may be inducing heat release via non-photochemical quenching, resulting in lower SIF. Besides canopy structure, the microclimate within these forests may also be exerting influence on SIF. We showed that LAI and foliage vertical distribution varies substantially across our disturbance classes (Figure 5), which leads to the creation of differential vertical microclimates. SIF and the absorbed photosynthetically active radiation (APAR) contributions from the lower and middle part of the canopy are likely higher in burned forests with a denser understory (Figure S4), and it remains elusive how they interact with the upper canopy and escape to be observed by sensors in space. Lastly, due to the complex interactions of SIF with the forest canopy, degradation status and SIF relationships across forest successional stages could be inconsistent. All those factors deserve further investigation.

We showed that the impact of fires on structure and SIF is much larger than impacts of selective logging. After the initial impact of fires and start of plant development, forests regenerating from fires maintain a high light-use efficiency (LUE, carbon fixed per unit light absorbed). One possible explanation for this phenomenon is that early-succession species (many of which are shrubs) are abundant in forests regenerating from fires, and have an ‘acquisitive resource capture strategy’, that grow fast and require high light levels (Poorter et al. 2004). These species develop cheap, short-lived leaves with high specific leaf area and photosynthetic rates to achieve fast growth (Bazzaz and Pickett 1980), investing more of the absorbed PAR to fix carbon through growth and photosynthesis (Both et al. 2019). Overall, the results of this study support the hypothesis that both logged and burned forests can rapidly (~ 4-7 years) recover productivity (e.g., Brando et al. 2019).

4.3 SIF and canopy structural complexity

We examined structural drivers of SIF in degraded and intact forests, focusing on four canopy structural aspects: canopy height, foliar distribution, and vertical and horizontal complexity. Although the existing SIF literature has highlighted the influence of canopy structural attributes, especially LAI, leaf angle distribution and fraction of sunlit leaves in SIF emissions during photosynthesis (Frankenberg and Berry 2018), this is the first time that the contribution of structural variables to tropical forests SIF variability is quantified explicitly.

The results of our modelling approach showed that the canopy height metrics (mean and standard deviation of returns, and standard deviation of 25th and 95th height percentiles) were the best set of explanatory variables of SIF (adjusted R^2 = 0.44). Lefsky et al. (2005) found that a combination of mean height of lidar returns, standard deviation of lidar returns, and degree of canopy closure were sufficient to accurately describe canopy structure of temperate needleleaf forests with strong correlation to coincident field measurements of forest functioning, such as LAI and aboveground biomass. d'Oliveira et al. (2012) found, for a logged tropical forest site in the Western Amazon, that the variance of lidar returns is related to both the variability of the canopy height and openness to passage of lidar pulses through foliage and branches. Thus, in this type of forest with highly variable canopy height, amplified by the canopy disturbances caused by forest degradation and subsequent regeneration, the standard deviation of lidar returns not only characterizes canopy surface variability and permeability, but to a large extent, canopy dominant height. These attributes are generic descriptors of canopy arrangement, and the inclusion of similar metrics in our best model suggests that they may perform as simplified proxies for more complex process controlling light harvesting in tropical forests.

The inclusion of sdP25 (negatively correlated to SIF, r = -0.35) and sdP95 (positively correlated to SIF, r = 0.25) metrics in the best canopy height model is an indication of the role of disturbance in SIF-structure relationships in our study area. These metrics are especially distinctive in areas affected by fires: sdP25 is low because the understory in these areas is homogeneously developing and constitute the greatest potential of light absorption (Figure 9, Figure S4). P95 is a descriptor of top-of-canopy height, and its standard deviation (sdP95) was greater in burned areas of different ages (Figure 9, Figure S3). Although slightly improving model performance, disturbance category was not a significant interaction term in the regression model. The disturbance category is not independent from the lidar metrics because most of the metrics contribute information about structural changes caused by disturbance.

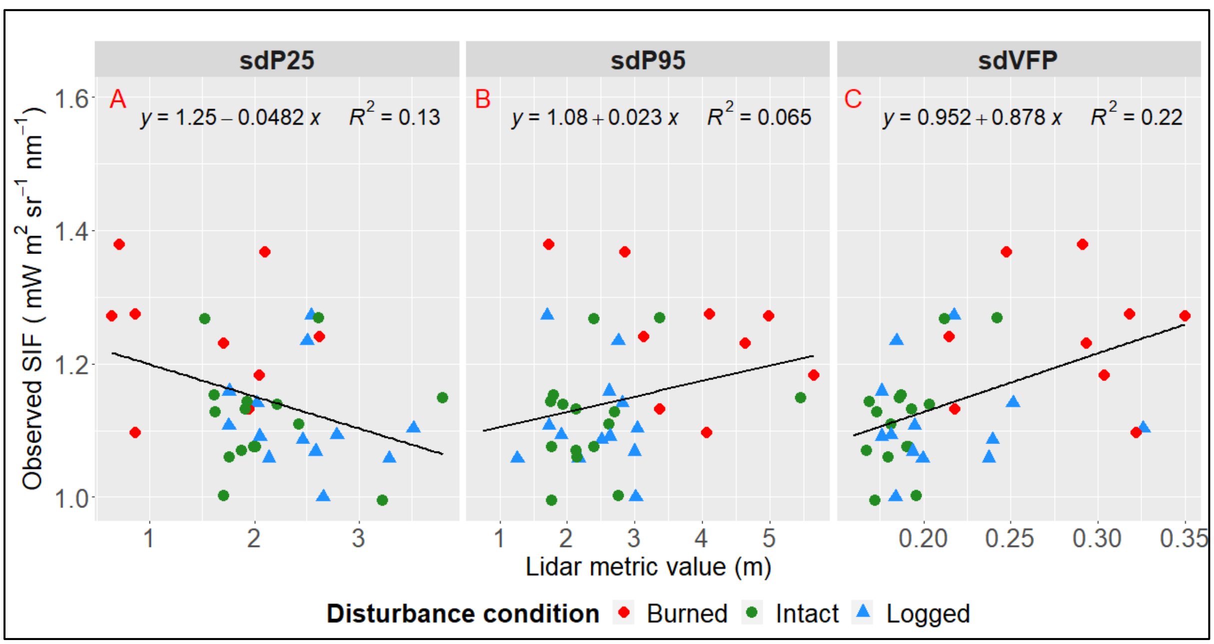

Figure 9. Relationship between SIF and sdP25, sdP95 and sdVFP lidar-derived metrics. The black line represents the best fit line.

Our findings showed that logging and fires induced heterogeneity in the canopy layering, and that this additional heterogeneity is also reflected in the variability of SIF, even though in an ambiguous manner. The inclusion of standard deviation metrics in the best explanatory models, and the facts that the standard deviation of the vertical foliage profile (sdVFP) was the best single predictor of SIF and that burned areas showed high sdVFP (Figure 9) with reduced LAI in some classes (e.g., B2, Figure 5) support this hypothesis.

Some mechanisms may be contributing to increased SIF in older burned areas during the wet season: first, recently burned areas may create niche opportunities for a grass flush (D'Antonio et al. 2001), and grass LAI is likely undetected or underestimated by airborne lidar. Second, SIF is primarily controlled by incoming PAR and, therefore, also quite sensitive to shadows (Mohammed et al. 2019). Third, the canopy structure of young forests is less complex and, therefore, the escape probability of SIF photons is higher. Köhler et al. (2018) argue that increased SIF and the canopy scattering coefficient of cropland and grassland areas might be explained by the rather less complex vegetation structure associated with an enhanced escape probability for scattered and emitted photons. By analogy, this mechanism also applies to the canopy of regenerating forests. We showed empirical evidence that burned areas in advanced regeneration have a more homogeneous canopy (Figure 5A), and hence, they are expected to have less shadow. Estimates of the sunlit and shaded leaves distribution at the time of SIF observations, can be estimated with models such as Discrete Anisotropic Radiative Transfer (DART), which could enhance the interpretation of these results (Gastellu-Etchegorry et al. 2015; Morton et al. 2016).

Disturbance does not only change the physical arrangement of canopy elements, but it also alters tree functional composition as successional processes take place (Cochrane and Schulze 1999; Ferry Slik et al. 2002; Rüger et al. 2020), and these species have higher photosynthetic capacity compared to late-successional species (Dusenge et al. 2015; Nogueira et al. 2004). In summary, there is a large amount of SIF variability (~56%) not explained by the structural metrics employed in this study that might be explained by plant physiology variables, as well as community and demographic dynamics following disturbances and their associated changes in structure. A recent model-based study by Rüger et al. (2020) suggested that tree functional composition change over succession (in terms of differentiation on growth–survival and stature–recruitment trade-offs) can explain forest structural change, highlighting the likely importance of community and demographic dynamics in forest transitions. In addition to leaf and wood traits, early-, mid- and late-successional trees are also distinguished by differences in canopy and whole plant architecture, features associated with light interception, tree growth rates, and vertical position within the forest canopy (Sterck and Bongers 2001). The assessment of canopy functional traits related to plant function (photosynthesis, respiration, evapotranspiration) via image spectroscopy could help to clarify these questions (Asner et al. 2017; Schimel and Schneider 2019).

We expect that regeneration following forest degradation will lead to increases in canopy complexity and SIF through time as observed in intact or second-growth forests (Gough et al. 2019; Hardiman et al. 2011). However, the pathways of regeneration and the resulting canopy structures in degraded tropical forests are more diverse and mostly poorly understood (Longo et al. 2020; Norden et al. 2015).

4.4 Limitations and prospects of the study

This study combined orbital and airborne remote sensing data to assess the relationship between forest structure and SIF. Despite substantial differences in the spatial resolution of the SIF (~ 5.5 km resolution) and small footprint airborne data (~ 30 cm footprint) and differences in the total area surveyed by the lidar transects compared to the TROPOMI footprint, we made a fundamental assumption that the lidar transects are representative of the vegetation captured in the

SIF data, and we took steps to minimize SIF pixel mixture. However, some significant differences in forest structure were not translated into differences in SIF, for instance, significantly lower LAI in the L2 class compared to intact forests did not show corresponding differences in the SIF data. There is a possibility of omission errors if selective logging is causing a change in SIF that we cannot detect because of both the subtle signal and the pixel purity issue. However, ground based studies (e.g., Miller et al. 2011) show that low intensity logging has a small effect on productivity and hence it probably has a small effect on SIF as well. Overall, we found that SIF alone was not sufficient to distinguish between intact and most of the anthropogenically disturbed forests, but the use of SIF data in conjunction with another dataset leveraged its potential. The advent of new SIF products with finer spatial resolution in the future and larger availability of lidar data such as the ongoing Global Ecosystem Dynamics Investigation (GEDI) orbital mission (Dubayah et al. 2020) or more extensive airborne lidar data acquisitions could bridge the gaps between those scales and further advance or refute our findings.

The sample size was also affected by the availability of lidar data and by the scale mismatch between SIF footprint and degradation polygons, especially logging. The most recent disturbance classes (L1 and L2, B1 and B2) comprise only four years each, leading to a smaller sample size compared to the L3 and B3 classes (Table 4) and consequently, larger uncertainty in structure and SIF estimates (Figure 5B, Figure 6). The adoption of the 70%-pixel purity threshold for each class was an attempt to tackle this issue, but we were still able to run comparative SIF analysis of degraded areas versus non-degraded areas and detected some differences. The mixing just diluted the signal contrast between the degraded versus non-degraded conditions.

An interesting aspect that arose from the lidar metrics was that top-of-canopy height and total LAI were in some cases lower in L2/B2 than in L1/B1. At this point, it is uncertain whether the low sample size or the LAD height threshold that we adopted (4.5m, that may increase LAD uncertainty at areas with high understory density) are driving this effect. Other plausible causes could be the increased mortality of large trees in the post-disturbance period, a well-documented phenomenon that occurs in degraded Amazon forests (Brando et al. 2019; Schulze and Zweede 2006). The occurrence of multiple disturbance events, severity of burns, and intensity of logging, aspects that have not been addressed in this study, could also be confounding our results.

An additional potential driver of uncertainty of this study is the temporal mismatch between remote sensing data acquisition dates and time of disturbances. Lidar collections follow contract schedules, while fire season and logging activities are usually related to the dry season in the Amazon. For instance, a lidar acquisition in April will not include most of the logging and fires disturbances for that year. Although we visually confirmed the degradation status of lidar transects based on the CHM, our disturbance classification still holds some degree of subjectivity, as we do not have a measure of classification accuracy. Moreover, for each pixel and band, the LandTrendr-based disturbance history classification selects the median value of all images considered in a year (Kennedy et al. 2010). Annual composite images based on such approach will likely fail to detect degradation events that happen late in the dry season of a given year, detecting them in the following year only.

5. Conclusion

Our study employed a combination of airborne lidar and SIF data and highlighted differences in ecosystem structure and function in a broad array of degraded sites. SIF showed positive or negative changes in degraded forests based on recent degradation and recovery history. By using spaceborne assets of forest function, our results show that combined observations improve our ability to detect the regional effects of forest degradation and indicate that anthropogenically disturbed forests can capture large amounts of carbon while recovering.

Acknowledgements

Lidar data were provided by the Sustainable Landscapes Brazil project, a collaboration of the Brazilian Agricultural Research Corporation (EMBRAPA), the US Forest Service, USAID, and the US Department of State; and by the Estimativas de Biomassa da Amazonia project (EBA_BNDES-Amazon Fund [Grant 14.2.0929.1]; the NAS and USAID [Grant AID-OAA-A-11-00012]. Funding source for TROPOMI: NASA Earth Science U.S. Participating Investigator [Grant Number NNX15AH95G]. The research carried out at the Jet Propulsion Laboratory, California Institute of Technology, was under a contract with the National Aeronautics and Space Administration. M. L. was supported by the NASA Postdoctoral Program, administered by Universities Space Research Association under contract with NASA and the Next Generation Ecosystem Experiments ‑ Tropics, funded by the U.S. Department of Energy, Office of Science, Office of Biological and Environmental Research. E. R. P. was supported by an Australian Government Research Training Program Scholarship, and by the USDA Forest Service Pacific Northwest Research Station and International Programs. We thank Danilo R. A. de Almeida for his support on the lidar data processing.

References

Aho, K., Derryberry, D., & Peterson, T. (2014). Model selection for ecologists: the worldviews of AIC and BIC. *Ecology, 95*, 631-636

Alencar, A.A., Brando, P.M., Asner, G.P., & Putz, F.E. (2015). Landscape fragmentation, severe drought, and the new Amazon forest fire regime. *Ecological Applications, 25*, 1493-1505

Almeida, D.R.A.d., Stark, S.C., Shao, G., Schietti, J., Nelson, B.W., Silva, C.A., Gorgens, E.B., Valbuena, R., Papa, D.d.A., & Brancalion, P.H.S. (2019). Optimizing the Remote Detection of Tropical Rainforest Structure with Airborne Lidar: Leaf Area Profile Sensitivity to Pulse Density and Spatial Sampling. *Remote Sensing, 11*, 92

Aragão, L.E., Poulter, B., Barlow, J.B., Anderson, L.O., Malhi, Y., Saatchi, S., Phillips, O.L., & Gloor, E. (2014). Environmental change and the carbon balance of Amazonian forests. *Biol Rev Camb Philos Soc, 89*, 913-931

Asner, G.P., Martin, R.E., Knapp, D.E., Tupayachi, R., Anderson, C.B., Sinca, F., Vaughn, N.R., & Llactayo, W. (2017). Airborne laser-guided imaging spectroscopy to map forest trait diversity and guide conservation. *Science, 355*, 385-389

Atkins, J.W., Fahey, R.T., Hardiman, B.S., & Gough, C.M. (2018). Forest Canopy Structural Complexity and Light Absorption Relationships at the Subcontinental Scale. *Journal of Geophysical Research: Biogeosciences, 123*, 1387-1405

Bazzaz, F., & Pickett, S. (1980). Physiological ecology of tropical succession: a comparative review. *Annual review of ecology and systematics, 11*, 287-310

Berenguer, E., Ferreira, J., Gardner, T.A., Aragão, L.E.O.C., De Camargo, P.B., Cerri, C.E., Durigan, M., Oliveira, R.C.D., Vieira, I.C.G., & Barlow, J. (2014). A large-scale field assessment of carbon stocks in human-modified tropical forests. *Global Change Biology, 20*, 3713-3726

Berenguer, E., Malhi, Y., Brando, P., Cordeiro, A.C.N., Ferreira, J., França, F., Rossi, L.C., Seixas, M.M.M.d., & Barlow, J. (2018). Tree growth and stem carbon accumulation in human-modified Amazonian forests following drought and fire. *Philosophical Transactions of the Royal Society B: Biological Sciences, 373*, 20170308

Bomfim, B., Silva, L.C.R., Marimon-Júnior, B.H., Marimon, B.S., Doane, T.A., & Horwath, W.R. (2020). Fire Affects Asymbiotic Nitrogen Fixation in Southern Amazon Forests. *Journal of Geophysical Research: Biogeosciences, 125*, e2019JG005383

Both, S., Riutta, T., Paine, C.E.T., Elias, D.M.O., Cruz, R.S., Jain, A., Johnson, D., Kritzler, U.H., Kuntz, M., Majalap-Lee, N., Mielke, N., Montoya Pillco, M.X., Ostle, N.J., Arn Teh, Y., Malhi, Y., & Burslem, D.F.R.P. (2019). Logging and soil nutrients independently explain plant trait expression in tropical forests. *New Phytologist, 221*, 1853-1865

Brando, P., Macedo, M., Silvério, D., Rattis, L., Paolucci, L., Alencar, A., Coe, M., & Amorim, C. (2020). Amazon wildfires: Scenes from a foreseeable disaster. *Flora*, 151609

Brando, P.M., Silvério, D., Maracahipes-Santos, L., Oliveira-Santos, C., Levick, S.R., Coe, M.T., Migliavacca, M., Balch, J.K., Macedo, M.N., Nepstad, D.C., Maracahipes, L., Davidson, E., Asner, G., Kolle, O., & Trumbore, S. (2019). Prolonged tropical forest degradation due to compounding disturbances: Implications for CO2 and H2O fluxes. *Global Change Biology, 25*, 2855-2868

Broadbent, E.N., Asner, G.P., Keller, M., Knapp, D.E., Oliveira, P.J.C., & Silva, J.N. (2008). Forest fragmentation and edge effects from deforestation and selective logging in the Brazilian Amazon. *Biological conservation, 141*, 1745-1757

Brum, M., Vadeboncoeur, M.A., Ivanov, V., Asbjornsen, H., Saleska, S., Alves, L.F., Penha, D., Dias, J.D., Aragão, L.E.O.C., Barros, F., Bittencourt, P., Pereira, L., & Oliveira, R.S. (2019). Hydrological niche segregation defines forest structure and drought tolerance strategies in a seasonal Amazon forest. *Journal of Ecology, 107*, 318-333

Bullock, E.L., Woodcock, C.E., Souza, C., & Olofsson, P. (2020). Satellite-based estimates reveal widespread forest degradation in the Amazon. *Global Change Biology, 26*, 2956-2969

Clark, D.B., Mercado, L.M., Sitch, S., Jones, C.D., Gedney, N., Best, M.J., Pryor, M., Rooney, G.G., Essery, R.L.H., Blyth, E., Boucher, O., Harding, R.J., Huntingford, C., & Cox, P.M. (2011). The Joint UK Land Environment Simulator (JULES), model description – Part 2: Carbon fluxes and vegetation dynamics. *Geosci. Model Dev., 4*, 701-722

Cochrane, M.A. (2003). Fire science for rainforests. *Nature, 421*, 913-919

Cochrane, M.A., & Schulze, M.D. (1999). Fire as a Recurrent Event in Tropical Forests of the Eastern Amazon: Effects on Forest Structure, Biomass, and Species Composition. *Biotropica, 31*, 2-16

D'Antonio, C.M., Hughes, R.F., & Vitousek, P.M. (2001). Factors influencing dynamics of two invasive C4 grasses in seasonally dry Hawaiian woodlands. *Ecology, 82*, 89-104

Dantas de Paula, M., Groeneveld, J., & Huth, A. (2015). Tropical forest degradation and recovery in fragmented landscapes — Simulating changes in tree community, forest hydrology and carbon balance. *Global Ecology and Conservation, 3*, 664-677

d'Oliveira, M.V., Reutebuch, S.E., McGaughey, R.J. & Andersen, H.-E. 2012, 'Estimating forest biomass and identifying low-intensity logging areas using airborne scanning lidar in Antimary State Forest, Acre State, Western Brazilian Amazon', *Remote Sensing of Environment*, vol. 124, pp. 479-91.

dos-Santos, M.N., Keller, M.M., & Morton, D.C. (2019). LiDAR Surveys over Selected Forest Research Sites, Brazilian Amazon, 2008-2018. In: ORNL Distributed Active Archive Center

Doughty, R., Köhler, P., Frankenberg, C., Magney, T.S., Xiao, X., Qin, Y., Wu, X., & Moore, B. (2019). TROPOMI reveals dry-season increase of solar-induced chlorophyll fluorescence in the Amazon forest. *Proceedings of the National Academy of Sciences*, 201908157

Drake, J.B., Dubayah, R.O., Clark, D.B., Knox, R.G., Blair, J.B., Hofton, M.A., Chazdon, R.L., Weishampel, J.F., & Prince, S. (2002). Estimation of tropical forest structural characteristics using large-footprint lidar. *Remote Sensing of Environment, 79*, 305-319

Dubayah, R., Blair, J.B., Goetz, S., Fatoyinbo, L., Hansen, M., Healey, S., Hofton, M., Hurtt, G., Kellner, J., Luthcke, S., Armston, J., Tang, H., Duncanson, L., Hancock, S., Jantz, P., Marselis, S., Patterson, P.L., Qi, W., & Silva, C. (2020). The Global Ecosystem Dynamics Investigation: High-resolution laser ranging of the Earth's forests and topography. *Science of Remote Sensing, 1*, 100002

Dusenge, M.E., Wallin, G., Gårdesten, J., Niyonzima, F., Adolfsson, L., Nsabimana, D., & Uddling, J. (2015). Photosynthetic capacity of tropical montane tree species in relation to leaf nutrients, successional strategy and growth temperature. *Oecologia, 177*, 1183-1194

Falkowski, M.J., Evans, J.S., Martinuzzi, S., Gessler, P.E., & Hudak, A.T. (2009). Characterizing forest succession with lidar data: An evaluation for the Inland Northwest, USA. *Remote Sensing of Environment, 113*, 946-956

Ferry Slik, J.W., Verburg, R.W., & Keßler, P.J.A. (2002). Effects of fire and selective logging on the tree species composition of lowland dipterocarp forest in East Kalimantan, Indonesia. *Biodiversity & Conservation, 11*, 85-98

Fox, J., & Weisberg, S. (2019). *An R Companion to Applied Regression* (Third Edition ed.). Sage

Frankenberg, C., & Berry, J. (2018). 3.10 - Solar Induced Chlorophyll Fluorescence: Origins, Relation to Photosynthesis and Retrieval. In S. Liang (Ed.), *Comprehensive Remote Sensing* (pp. 143-162). Oxford: Elsevier

Frankenberg, C., O'Dell, C., Guanter, L., & McDuffie, J. (2012). Remote sensing of near-infrared chlorophyll fluorescence from space in scattering atmospheres: implications for its retrieval and interferences with atmospheric CO₂ retrievals. *Atmos. Meas. Tech., 5*, 2081-2094

Gastellu-Etchegorry, J.-P., Yin, T., Lauret, N., Cajgfinger, T., Gregoire, T., Grau, E., Feret, J.-B., Lopes, M., Guilleux, J., Dedieu, G., Malenovský, Z., Cook, B.D., Morton, D., Rubio, J., Durrieu, S., Cazanave, G., Martin, E., & Ristorcelli, T. (2015). Discrete Anisotropic Radiative Transfer (DART 5) for Modeling Airborne and Satellite Spectroradiometer and LIDAR Acquisitions of Natural and Urban Landscapes. *Remote Sensing, 7*, 1667-1701

Gough, C.M., Atkins, J.W., Fahey, R.T., & Hardiman, B.S. (2019). High rates of primary production in structurally complex forests. *Ecology, 100*, e02864

Hardiman, B.S., Bohrer, G., Gough, C.M., Vogel, C.S., & Curtis, P.S. (2011). The role of canopy structural complexity in wood net primary production of a maturing northern deciduous forest. *Ecology, 92*, 1818-1827

Huete, A., Didan, K., Miura, T., Rodriguez, E.P., Gao, X., & Ferreira, L.G. (2002). Overview of the radiometric and biophysical performance of the MODIS vegetation indices. *Remote Sensing of Environment, 83*, 195-213

Huete, A.R., Didan, K., Shimabukuro, Y.E., Ratana, P., Saleska, S.R., Hutyra, L.R., Yang, W., Nemani, R.R., & Myneni, R. (2006). Amazon rainforests green-up with sunlight in dry season. *Geophysical Research Letters, 33*

IBGE 2021, 'Mapeamento de Recursos Naturais do Brasil - Escala 1:250.000 - Versão 2021', electronic data set, viewed January 14, 2022, <https://www.ibge.gov.br/geociencias/informacoes-ambientais/vegetacao/22453-cartas-1-250-000.html?=&t=downloads>.

INPE (2020). PRODES - Monitoramento da Floresta Amazônica por Satélite. In. São José dos Campos, Brazil: National Institute for Space Research

Kamoske, A.G., Dahlin, K.M., Stark, S.C., & Serbin, S.P. (2019). Leaf area density from airborne LiDAR: Comparing sensors and resolutions in a temperate broadleaf forest ecosystem. *Forest Ecology and Management, 433*, 364-375

Kane, V.R., Bakker, J.D., McGaughey, R.J., Lutz, J.A., Gersonde, R.F., & Franklin, J.F. (2010). Examining conifer canopy structural complexity across forest ages and elevations with LiDAR data. *Canadian Journal of Forest Research, 40*, 774-787

Kennedy, R.E., Yang, Z., & Cohen, W.B. (2010). Detecting trends in forest disturbance and recovery using yearly Landsat time series: 1. LandTrendr—Temporal segmentation algorithms. *Remote Sensing of Environment, 114*, 2897-2910

Kennedy, R.E., Yang, Z., Gorelick, N., Braaten, J., Cavalcante, L., Cohen, W.B., & Healey, S. (2018). Implementation of the LandTrendr Algorithm on Google Earth Engine. *Remote Sensing, 10*, 691

Kim, J., Ryu, Y., Dechant, B., Lee, H., Kim, H.S., Kornfeld, A., & Berry, J.A. (2021). Solar-induced chlorophyll fluorescence is non-linearly related to canopy photosynthesis in a temperate evergreen needleleaf forest during the fall transition. *Remote Sensing of Environment, 258*, 112362

Knapp, N., Fischer, R., Cazcarra-Bes, V., & Huth, A. (2020). Structure metrics to generalize biomass estimation from lidar across forest types from different continents. *Remote Sensing of Environment, 237*, 111597

Koffi, E.N., Rayner, P.J., Norton, A.J., Frankenberg, C., & Scholze, M. (2015). Investigating the usefulness of satellite-derived fluorescence data in inferring gross primary productivity within the carbon cycle data assimilation system. *Biogeosciences, 12*, 4067-4084

Köhler, P., Frankenberg, C., Magney, T.S., Guanter, L., Joiner, J., & Landgraf, J. (2018a). Global Retrievals of Solar-Induced Chlorophyll Fluorescence With TROPOMI: First Results and Intersensor Comparison to OCO-2. *Geophysical Research Letters, 45*, 10,456-410,463

Köhler, P., Guanter, L., Kobayashi, H., Walther, S., & Yang, W. (2018b). Assessing the potential of sun-induced fluorescence and the canopy scattering coefficient to track large-scale vegetation dynamics in Amazon forests. *Remote Sensing of Environment, 204*, 769-785

Lefsky, M., Cohen, W.B., Parker, G., & Harding, D.J. (2002). Lidar Remote Sensing for Ecosystem Studies. *BioScience, 52*, 19-30

Lefsky, M.A., Hudak, A.T., Cohen, W.B., & Acker, S. (2005). Geographic variability in lidar predictions of forest stand structure in the Pacific Northwest. *Remote Sensing of Environment, 95*, 532-548

Lima, A., Silva, T.S.F., Aragão, L.E.O.e.C.d., Feitas, R.M.d., Adami, M., Formaggio, A.R., & Shimabukuro, Y.E. (2012). Land use and land cover changes determine the spatial relationship between fire and deforestation in the Brazilian Amazon. *Applied Geography, 34*, 239-246

Longo, M., Keller, M., dos-Santos, M.N., Leitold, V., Pinagé, E.R., Baccini, A., Saatchi, S., Nogueira, E.M., Batistella, M., & Morton, D.C. (2016). Aboveground biomass variability across intact and degraded forests in the Brazilian Amazon. *Global Biogeochemical Cycles, 30*, 1639-1660

Longo, M., Saatchi, S., Keller, M., Bowman, K., Ferraz, A., Moorcroft, P.R., Morton, D.C., Bonal, D., Brando, P., Burban, B., Derroire, G., dos-Santos, M.N., Meyer, V., Saleska, S., Trumbore, S., & Vincent, G. (2020). Impacts of Degradation on Water, Energy, and Carbon Cycling of the Amazon Tropical Forests. *Journal of Geophysical Research: Biogeosciences, 125*, e2020JG005677

MacArthur, R.H., & Horn, H.S. (1969). Foliage profile by vertical measurements. *Ecology, 50*, 802-804

MapBiomas Project 2019, *The Brazilian Annual Land Use and Land Cover Mapping Project – Collection 4.0* Brasilia, viewed September 12 2019, <https://mapbiomas.org/en>.

Matricardi, E.A., Skole, D.L., Pedlowski, M.A., Chomentowski, W., & Fernandes, L.C. (2010). Assessment of tropical forest degradation by selective logging and fire using Landsat imagery. *Remote Sensing of Environment, 114*, 1117-1129

McGaughey, R.J. (2015). FUSION/LDV: Software for LIDAR Data Analysis and Visualization. In (p. 186). Seattle, WA: Pacific Northwest Research Station - United States Forest Service

Miller, A.J. (1984). Selection of Subsets of Regression Variables. *Journal of the Royal Statistical Society. Series A (General), 147*, 389-425

Miller, S.D., Goulden, M.L., Hutyra, L.R., Keller, M., Saleska, S.R., Wofsy, S.C., Figueira, A.M.S., da Rocha, H.R., & de Camargo, P.B. (2011). Reduced impact logging minimally alters tropical rainforest carbon and energy exchange. *Proceedings of the National Academy of Sciences, 108*, 19431-19435Mohammed, G.H., Colombo, R., Middleton, E.M., Rascher, U., van der Tol, C., Nedbal, L., Goulas, Y., Pérez-Priego, O., Damm, A., Meroni, M., Joiner, J., Cogliati, S., Verhoef, W., Malenovský, Z., Gastellu-Etchegorry, J.-P., Miller, J.R., Guanter, L., Moreno, J., Moya, I., Berry, J.A., Frankenberg, C., & Zarco-Tejada, P.J. (2019). Remote sensing of solar-induced chlorophyll fluorescence (SIF) in vegetation: 50 years of progress. *Remote Sensing of Environment, 231*, 111177

Moran, E.F. (1993). Deforestation and land use in the Brazilian Amazon. *Human Ecology, 21*, 1-21

Morton, D., Le Page, Y., DeFries, R., Collatz, G., & Hurtt, G. (2013). Understorey fire frequency and the fate of burned forests in southern Amazonia. *Philosophical Transactions of the Royal Society B: Biological Sciences, 368*, 20120163

Morton, D.C., Rubio, J., Cook, B.D., Gastellu-Etchegorry, J.P., Longo, M., Choi, H., Hunter, M., & Keller, M. (2016). Amazon forest structure generates diurnal and seasonal variability in light utilization. *Biogeosciences, 13*, 2195-2206

Nepstad, D.C., de Carvalho, C.R., Davidson, E.A., Jipp, P.H., Lefebvre, P.A., Negreiros, G.H., da Silva, E.D., Stone, T.A., Trumbore, S.E., & Vieira, S. (1994). The role of deep roots in the hydrological and carbon cycles of Amazonian forests and pastures. *Nature, 372*, 666-669

Nogueira, A., Martinez, C.A., Ferreira, L.L., & Prado, C.H.B.A. (2004). Photosynthesis and Water Use Efficiency in Twenty Tropical Tree Species of Differing Succession Status in a Brazilian Reforestation. *Photosynthetica, 42*, 351-356

Norden, N., Angarita, H.A., Bongers, F., Martínez-Ramos, M., Granzow-de la Cerda, I., van Breugel, M., Lebrija-Trejos, E., Meave, J.A., Vandermeer, J., Williamson, G.B., Finegan, B., Mesquita, R., & Chazdon, R.L. (2015). Successional dynamics in Neotropical forests are as uncertain as they are predictable. *Proceedings of the National Academy of Sciences, 112*, 8013-8018

Odum, E.P. (1969). The Strategy of Ecosystem Development. *Science, 164*, 262-270

Ordway, E.M., & Asner, G.P. (2020). Carbon declines along tropical forest edges correspond to heterogeneous effects on canopy structure and function. *Proceedings of the National Academy of Sciences, 117*, 7863-7870

Parazoo, N.C., Bowman, K., Fisher, J.B., Frankenberg, C., Jones, D.B.A., Cescatti, A., Pérez-Priego, Ó., Wohlfahrt, G., & Montagnani, L. (2014). Terrestrial gross primary production inferred from satellite fluorescence and vegetation models. *Global Change Biology, 20*, 3103-3121

Parker, G.G., & Russ, M.E. (2004). The canopy surface and stand development: assessing forest canopy structure and complexity with near-surface altimetry. *Forest Ecology and Management, 189*, 307-315

Porcar-Castell, A. (2011). A high-resolution portrait of the annual dynamics of photochemical and non-photochemical quenching in needles of Pinus sylvestris. *Physiologia Plantarum, 143*, 139-153

Poorter, L., Van de Plassche, M., Willems, S., & Boot, R. (2004). Leaf traits and herbivory rates of tropical tree species differing in successional status. *Plant biology, 6*, 746-754

Prestes, N.C.C.d.S., Massi, K.G., Silva, E.A., Nogueira, D.S., de Oliveira, E.A., Freitag, R., Marimon, B.S., Marimon-Junior, B.H., Keller, M., & Feldpausch, T.R. (2020). Fire Effects on Understory Forest Regeneration in Southern Amazonia. *Frontiers in Forests and Global Change, 3*

R Core Team (2019). R: A language and environment for statistical computing. In. Vienna, Austria: R Foundation for Statistical Computing

RADAMBRASIL, P. (1983). Projeto RADAMBRASIL: 1973–1983, Levantamento de Recursos Naturais. In M.d.M.e. Energia, & Departamento Nacional de Produção Mineral (DNPM) (Eds.). Rio de Janeiro

Rangel Pinagé, E., Keller, M., Duffy, P., Longo, M., dos-Santos, M.N., & Morton, D.C. (2019). Long-Term Impacts of Selective Logging on Amazon Forest Dynamics from Multi-Temporal Airborne LiDAR. *Remote Sensing, 11*, 709

Rappaport, D.I., Morton, D.C., Longo, M., Keller, M., Dubayah, R., & dos-Santos, M.N. (2018). Quantifying long-term changes in carbon stocks and forest structure from Amazon forest degradation. *Environmental Research Letters, 13*, 065013

Rouse Jr, J.W., Haas, R., Schell, J., & Deering, D. (1974). Monitoring vegetation systems in the Great Plains with ERTS. In S.C. Freden, Mercanti, E.P., Becker, M.. (Ed.), *Third Earth Resources Technology Satellite–1 Symposium* (pp. 309-317). Washington, D.C., USA: NASA SP-351

Roussel, J.-R., Auty, D., Coops, N.C., Tompalski, P., Goodbody, T.R.H., Meador, A.S., Bourdon, J.-F., de Boissieu, F., & Achim, A. (2020). lidR: An R package for analysis of Airborne Laser Scanning (ALS) data. *Remote Sensing of Environment, 251*, 112061

Rüger, N., Condit, R., Dent, D.H., DeWalt, S.J., Hubbell, S.P., Lichstein, J.W., Lopez, O.R., Wirth, C., & Farrior, C.E. (2020). Demographic trade-offs predict tropical forest dynamics. *Science, 368*, 165-168

Savitzky, A., & Golay, M.J. (1964). Smoothing and differentiation of data by simplified least squares procedures. *Analytical chemistry, 36*, 1627-1639

Scaranello, M.A.S., Keller, M., Longo, M., dos-Santos, M.N., Leitold, V., Morton, D.C., Pinagé, E.R., & Espírito-Santo, F.D.B. (2019). Estimation of coarse dead wood stocks in intact and degraded forests in the Brazilian Amazon using airborne lidar. *Biogeosciences, 16*, 3457-3474

Schimel, D., & Schneider, F.D. (2019). Flux towers in the sky: global ecology from space. *New Phytologist, 224*, 570-584

Schulze, M., & Zweede, J. (2006). Canopy dynamics in unlogged and logged forest stands in the eastern Amazon. *Forest Ecology and Management, 236*, 56-64

Silva, C.V.J., Aragão, L.E.O.C., Barlow, J., Espirito-Santo, F., Young, P.J., Anderson, L.O., Berenguer, E., Brasil, I., Foster Brown, I., Castro, B., Farias, R., Ferreira, J., França, F., Graça, P.M.L.A., Kirsten, L., Lopes, A.P., Salimon, C., Scaranello, M.A., Seixas, M., Souza, F.C., & Xaud, H.A.M. (2018). Drought-induced Amazonian wildfires instigate a decadal-scale disruption of forest carbon dynamics. *Philosophical Transactions of the Royal Society B: Biological Sciences, 373*

Smith, M.N., Stark, S.C., Taylor, T.C., Ferreira, M.L., de Oliveira, E., Restrepo-Coupe, N., Chen, S., Woodcock, T., dos Santos, D.B., Alves, L.F., Figueira, M., de Camargo, P.B., de Oliveira, R.C., Aragão, L.E.O.C., Falk, D.A., McMahon, S.M., Huxman, T.E., & Saleska, S.R. (2019). Seasonal and drought-related changes in leaf area profiles depend on height and light environment in an Amazon forest. *New Phytologist, 222*, 1284-1297

Souza Jr, C.M., Siqueira, J.V., Sales, M.H., Fonseca, A.V., Ribeiro, J.G., Numata, I., Cochrane, M.A., Barber, C.P., Roberts, D.A., & Barlow, J. (2013). Ten-year Landsat classification of deforestation and forest degradation in the Brazilian Amazon. *Remote Sensing, 5*, 5493-5513

Stark, S.C., Leitold, V., Wu, J.L., Hunter, M.O., de Castilho, C.V., Costa, F.R.C., McMahon, S.M., Parker, G.G., Shimabukuro, M.T., Lefsky, M.A., Keller, M., Alves, L.F., Schietti, J., Shimabukuro, Y.E., Brandão, D.O., Woodcock, T.K., Higuchi, N., de Camargo, P.B., de Oliveira, R.C., & Saleska, S.R. (2012). Amazon forest carbon dynamics predicted by profiles of canopy leaf area and light environment. *Ecology Letters, 15*, 1406-1414

Sterck, F.J., & Bongers, F. (2001). Crown development in tropical rain forest trees: patterns with tree height and light availability. *Journal of Ecology, 89*, 1-13

Sun, Y., Frankenberg, C., Jung, M., Joiner, J., Guanter, L., Köhler, P., & Magney, T. (2018). Overview of Solar-Induced chlorophyll Fluorescence (SIF) from the Orbiting Carbon Observatory-2: Retrieval, cross-mission comparison, and global monitoring for GPP. *Remote Sensing of Environment, 209*, 808-823

Tang, H., & Dubayah, R. (2017). Light-driven growth in Amazon evergreen forests explained by seasonal variations of vertical canopy structure. *Proceedings of the National Academy of Sciences*, 201616943

Tyukavina, A., Hansen, M.C., Potapov, P.V., Stehman, S.V., Smith-Rodriguez, K., Okpa, C., & Aguilar, R. (2017). Types and rates of forest disturbance in Brazilian Legal Amazon, 2000–2013. *Science Advances, 3*, e1601047

Valbuena, R., Maltamo, M., Mehtätalo, L., & Packalen, P. (2017). Key structural features of Boreal forests may be detected directly using L-moments from airborne lidar data. *Remote Sensing of Environment, 194*, 437-446

van Ewijk, K., Treitz, P., & Scott, N. (2011). Characterizing Forest Succession in Central Ontario using LiDAR derived Indices. *Photogrammetric Engineering and Remote Sensing, 77*, 261-270

Vaughn, N.R., Asner, G.P., & Giardina, C.P. (2015). Long-term fragmentation effects on the distribution and dynamics of canopy gaps in a tropical montane forest. *Ecosphere, 6*, 1-15

Venables, W., & Ripley, B. (2002). Modern Applied Statistics with S. Springer-Verlag. *New York*

Verrelst, J., Rivera, J.P., van der Tol, C., Magnani, F., Mohammed, G., & Moreno, J. (2015). Global sensitivity analysis of the SCOPE model: what drives simulated canopy-leaving sun-induced fluorescence? *Remote Sensing of Environment, 166*, 8-21

Villa, P.M., Martins, S.V., Oliveira Neto, S.N.d., Rodrigues, A.C., Safar, N.V.H., Monsanto, L.D., Cancio, N.M., & Ali, A. (2018). Woody species diversity as an indicator of the forest recovery after shifting cultivation disturbance in the northern Amazon. *Ecological Indicators, 95*, 687-694

Wu, J., Albert, L.P., Lopes, A.P., Restrepo-Coupe, N., Hayek, M., Wiedemann, K.T., Guan, K., Stark, S.C., Christoffersen, B., Prohaska, N., Tavares, J.V., Marostica, S., Kobayashi, H., Ferreira, M.L., Campos, K.S., da Silva, R., Brando, P.M., Dye, D.G., Huxman, T.E., Huete, A.R., Nelson, B.W., & Saleska, S.R. (2016). Leaf development and demography explain photosynthetic seasonality in Amazon evergreen forests. *Science, 351*, 972-976

Zhang, Z.D., Zang, R.G., & Qi, Y.D. (2008). Spatiotemporal patterns and dynamics of species richness and abundance of woody plant functional groups in a tropical forest landscape of Hainan Island, South China. *J Integr Plant Biol, 50*, 547-558

Zuromski, L.M., Bowling, D.R., Köhler, P., Frankenberg, C., Goulden, M.L., Blanken, P.D., & Lin, J.C. (2018). Solar-Induced Fluorescence Detects Interannual Variation in Gross Primary Production of Coniferous Forests in the Western United States. *Geophysical Research Letters, 45*, 7184-7193

List of Figure Captions

Figure 1. Location (A), land cover (B, INPE 2020) and monthly precipitation (C) of the study area. Source of precipitation data: climate-data.org.

Figure 2. Overview of the major analysis steps and data sources. Blue boxes and arrows refer to forest structure, green boxes and arrows refer to SIF, black boxes and arrows refer to the disturbance history classification, and red boxes and arrows refer to the integrative analysis of structure and SIF.

Figure 3. Example of SIF grid cell selection (intact at green, logged at blue and burned forests at orange inset) according to pixel mixture and availability of lidar transect. Background images are NBR annual composites from 2019 (main map and intact forest inset), 2016 (logged forest inset) and 2010 (burned forest inset). Lighter areas in the NBR image represent dense canopy cover, while darker areas represent low or no canopy cover. Degradation by fire or logging appears in intermediate grey tones.

Figure 4. Lidar-derived canopy height models and associated density plots of 8-ha sample plots for each disturbance class.

Figure 5. Panel A: Vertical foliage profile for the disturbance classes. Intact forest's LAD is plotted over logged and burned forests' plots as a reference. Bands along the lines represent the standard error. Panel B: Distribution of leaf area index (LAI) above 4.5m for the disturbance classes. The violin plots summarize LAI distributions as a function of disturbance class and show the kernel probability density of the data at different values. All violins have the same area. The median of each group is indicated by the white dots. The symbols on the top indicate statistical significance (p-values, ns = $p > 0.05$; * = $p \leq 0.05$; ** $p \leq 0.01$) as computed from the multiple pairwise test against a reference group (IN, intact forests).

Figure 6. SIF time-series (daily data averaged to 16-days) for the disturbed classes with intact forests time-series as reference. The included period is March 1st, 2018, to September 30th, 2019. Beige shades indicate the dry season (months with <100mm precipitation) in the study area. Lines represent the median value of the 16-days average. The bands represent the 95% confidence interval for the median and provide an indication of whether the estimates of SIF for intact and disturbed forests overlap. Disturbance classes are intact forests (IN), 0-3 years (B1), 4-7 years (B2), and 8-14 (B3) years after fires, and 0-3 years (L1), 4-7 years (L2), and 8-14 (L3) years after logging.

Figure 7. Comparison of averaged SIF values between intact and disturbed forests across wet and dry seasons. Coloured lines represent the best fit, black dashed lines indicate the 1:1 line, and grey bands represent 95% confidence intervals. Disturbance classes are intact forests (IN), 0-3 years (B1), 4-7 years (B2), and 8-14 (B3) years after fires, and 0-3 years (L1), 4-7 years (L2), and 8-14 (L3) years after logging.

Figure 8. Observed versus predicted values of SIF as estimated by the models. Each dot represents the median value of SIF observations across the months of April-June 2018 and the SIF value predicted from lidar metrics for a given 'pure SIF pixel'. Dashed line is the 1:1 line, and r values represent the Pearson correlation coefficient between observed and predicted values.

Figure 9. Relationship between SIF and sdP25, sdP95 and sdVFP lidar-derived metrics. The black line represents the best fit line.